Phase-field modeling of hydraulic fracture

CrossMark

Zachary A. Wilson, Chad M. Landis *

Department of Aerospace Engineering and Engineering Mechanics and, The Institute for Computational Engineering and Science, The University of Texas at Austin, 210 East 24th Street, C0600, Austin, TX 78712-1221, United States

ARTICLE INFO

ABSTRACT

In this work a theoretical framework implementing the phase-field approach to fracture is used to couple the physics of flow through porous media and cracks with the mechanics of fracture. The main modeling challenge addressed in this work, which is a challenge for all diffuse crack representations, is on how to allow for the flow of fluid and the action of fluid pressure on the aggregate within the diffuse damage zone of the cracks. The theory is constructed by presenting the general physical balance laws and conducting a consistent thermodynamic analysis to constrain the constitutive relationships. Constitutive equations that reproduce the desired responses at the various limits of the phase-field parameter are proposed in order to capture Darcy-type flow in the intact porous medium and Stokes-type flow within open cracks. A finite element formulation for the solution of the governing model equations is presented and discussed. Finally, the theoretical and numerical model is shown to compare favorably to several important analytical solutions. More complex and interesting calculations are also presented to illustrate some of the advantageous features of the approach.

© 2016 Elsevier Ltd. All rights reserved.

1. Introduction

The method of propagating fractures with hydraulically pressurized fluids is common in many engineering applications, particularly in the field of geology. Certainly the most notable of these is the stimulation of oil and gas wells, but other applications include waste disposal (Bell, 2004), in situ stress measurement (Aamodt and Kuriyagawa, 1981), the stimulation of ground water wells (Banks et al., 1996; Less and Andersen, 1994), and geothermal reservoir development (Ghassemi, 2012). The advent of massive hydraulic fracturing and horizontal drilling in recent decades has made the extraction of oil and gas from unconventional reservoirs, particularly shale, economically viable. Additionally, heat extraction from sub-surface geothermal systems has the potential to be a significant source of renewable carbon-free energy both world-wide and in the U.S. (Bertani, 2012; Matek, 2015). As such, the optimization of the many applications related to fluid driven fracturing is becoming increasingly important.

Conventional modeling approaches to hydraulically fractured systems have assumed symmetric, planar, bi-wing crack geometries. Analytical 2D models were developed that made use of simplifying geometrical assumptions for fracture height and width in order to arrive at solutions in closed form. One such model, the Perkins-Kern-Nordgren (PKN) model, was formulated for fractures where the crack height is much smaller than crack length. The crack cross-section was assumed to be elliptical and to maintain a constant height along the length of the crack (Perkins and Kern, 1961; Nordgren, 1972).

---

* Corresponding author.
 E-mail address: landis@utexas.edu (C.M. Landis).

Another popular model, named after the work by Kristianovic, Geertsma, and de Klerk (KGD), was formulated for fractures where the crack height is much larger than crack length. In this case the crack cross section was assumed to have constant width (Geertsma and De Klerk, 1969; Daneshy, 1973). The coupling of these simplifying geometrical assumptions with fluid mass conservation and the Poiseuille law for the fluid flow in the cracks yielded closed form solutions for the crack growth history. Both models have also been modified to include leak-off of the pressurized fluid into the surrounding porous rock. Later, planar three-dimensional and pseudo-three-dimensional computational models were developed that incorporate anisotropic fracture properties of the rock layers to predict more complex fracture height, length, and width growth profiles (Settari and Cleary, 1986; Adachi et al., 2007). Several commercial production codes are based on these ideas and are in use today (Adachi et al., 2007). Additional studies, most notably by Detournay and co-workers (Detournay, 2004; Detournay and Peirce, 2014; Desroches et al., 1994), have revisited planar crack geometries, plane strain and penny shape cracks, and carefully investigated the crack tip behavior and propagation regimes of hydraulic fractures. These asymptotic analyses and analytical solutions provide valuable insights into some of the fundamental behaviors of fluid driven fractures and supply test cases for comparison with numerical methods developed for more complex crack surface evolutions.

Recently research efforts have largely shifted towards the modeling of more complex fracture geometries. Microseismic mappings performed on hydraulically fractured wells have revealed that complex fracture growth is more prevalent than had been initially estimated and that such phenomena occur with increased frequency in unconventional reservoirs (Cipolla et al., 2012; Mayerhofer et al., 2010). In particular, induced hydraulic fractures interact with pre-existing propped and natural fractures as well as other anisotropic features and inhomogeneities in the material (Roussel and Sharma, 2011; Olson and Wu, 2012). Due to the low permeability of unconventional reservoirs, a proper understanding of fracture evolution is paramount to evaluating and ensuring the desired production of the well. Many of the same issues exist for enhanced geothermal reservoir development along with the additional complications associated with thermal effects and the generation of thermal cracks. Ultimately, the production of energy resources from these types of reservoirs can be improved with the development and utilization of high fidelity numerical tools that model the coupled fluid, thermal, and mechanical behaviors properly while allowing for complex crack growth topologies and interactions.

There exists several works on the numerical modeling of the fluid driven fracture process. Many of these approaches assume that the network of potential crack paths is known, e.g. a rectangular lattice of potential crack surfaces exists a priori, and the fluid loading then acts to open parts of said network as the fluid injection process proceeds (Zhang et al., 2008; Zhang and Jeffrey, 2008; Zhang et al., 2007; Fu et al., 2013; Warpinski et al., 2009; Meyer and Bazan, 2011; Weng et al., 2011). The method developed in this work seeks to address cases where the crack path is not known a priori. Other approaches for generic crack path evolution also exist, and each is thought to have certain strengths and weaknesses. Overall, the methods can be grouped into two types of approaches: (i) sharp interface methods where the cracks are represented explicitly and thus require constitutive rules for crack propagation and (ii) diffuse crack models where a significant challenge resides in representing physical behaviors within the cracks like the pressure and flow of fluids.

Of note for sharp interface methods are boundary element methods (Rungamornrat et al., 2005) and discrete crack representations within finite element methods (Dahi-Taleghani and Olson, 2011; Gu et al., 2011; Khoei and Haghighat, 2001; Khoei et al., 2014; Pereira et al., 2010; Rangarajan and Lew, 2014; Rangarajan et al., 2014). Boundary element methods for determining the evolution of complex crack patterns have the advantage of being highly computationally efficient. Meshes are only needed on the boundaries of the domain and on the crack surfaces. Growth laws for the crack front are postulated relating the front velocity and direction to the local stress intensity factors. The disadvantages of the method are associated with difficulties for the incorporation of nonlinear or time dependent material responses in the bulk elastic material, and also in the handling of topological changes in the crack growth evolution like crack merging or branching. The discrete crack finite element methods usually implement numerical enrichment functions to allow cracks to grow through elements (Khoei et al., 2014; Pereira et al., 2010) or they relocate nodal positions such that cracks grow along element boundaries (Rangarajan and Lew, 2014). Both approaches also implement special element types at the crack front in order to capture the linear elastic near-tip K-fields for elastic problems. Such finite element methods will of course allow for nonlinear and time-dependent behavior in the bulk material, although any nonlinear behavior affecting the crack tip fields may negate the utility of using the special crack tip elements and any crack growth laws based upon the stress intensities. While the topological changes associated with crack merging and branching can be addressed using level set methods and remeshing, the necessity of additional constitutive rules for crack branching, direction selection, and nucleation remain.

Examples of diffuse crack approaches include peridynamics (Ha and Bobaru, 2010; Ouchi et al., 2015), gradient damage mechanics (Lorentz et al., 2012; Shojaei et al., 2014), and the phase-field methods presented herein and by other recent studies (Amor et al., 2009; Bourdin, 2007; Bourdin et al., 2000; Bourdin et al., 2008; Bourdin et al., 2011; Del Piero et al., 2007; Francfort and Marigo, 1998; Hofacker and Miehe, 2013; Miehe et al., 2010; Borden et al., 2012; Borden et al., 2014; Karma et al., 2001; Henry and Levine, 2004). Peridynamics is a nonlocal theory in which material points interact with all other material points that reside within a nearby "horizon". As with the phase-field method, cracks are not tracked explicitly but rather emerge naturally from the model equations. Gradient damage mechanics approaches and phase-field fracture approaches are very similar with minor differences in the details of how localization occurs and the length scale over which damage is able to spread. All of these diffuse crack methods alleviate many of the issues related to the topological changes in crack path evolutions associated with branching, turning, merging, and nucleation. However, there are challenges associated with modeling the fluid flow through cracks and the interaction of pressurized fluids with crack faces.

The phase-field methodology has emerged as a powerful tool for modeling the evolution of microstructures and the interactions of defects in a wide range of materials and physical processes (Provotas et al., 1998; Chen, 2002; Koslowski et al., 2002; Zhang and Bhattacharya, 2005; Su and Landis, 2007). Phase-field methods can be implemented to simulate large-scale evolution of material microstructure and defect motion without the need to explicitly track interfaces or defects. One strength of this modeling approach lies in the fact that there are no additional constitutive rules required within the theory that dictate when a crack should nucleate, grow, change direction, or split into multiple cracks. Cracks and their growth emerge as solutions to the governing partial differential equations of the model. A particularly unique and striking feature of the approach is that all calculations are performed entirely on the initial, undeformed configuration. There is no need to disconnect, eliminate, or move elements or introduce additional discontinuous basis functions, as is commonly done in the discrete crack computational fracture mechanics approaches. This results in a significant simplification of the numerical implementation, and a simple and direct pathway from two-dimensional to three-dimensional applications.

The purpose of this work is to enhance the phase-field/variational approach to fracture by coupling the physics of flow through porous media and cracks with the mechanics of fracture. The main modeling challenge addressed in this work, which is a challenge for all diffuse crack representations, is on how to allow for the flow of fluid and the action of fluid pressure on the aggregate within the diffuse damage zone of the cracks. There have been a few very recent studies which address the implementation of the phase-field method for fracture in poroelastic media (Bourdin et al., 2012; Miehe et al., 2015; Mikelic et al., 2015). The primary distinction in this work is in the presentation of the governing balance laws, and then the development of constitutive relationships through Coleman and Noll-type analysis procedures and, in particular, the handling of the fluid flow equations, which recover the Stokes equations for the fluid flow within cracks. We begin by developing the general balance laws and conducting a thorough thermodynamic analysis. We then propose constitutive equations that reproduce the desired responses at the various limits of the phase-field variable. In Section 3, we summarize our model equations and outline the numerical methods used to solve the equations. Finally, in Section 4, the approach developed is shown to compare favorably to several important analytical solutions. More complex and interesting calculations are also presented to illustrate some of the advantageous features of the approach.

2. General theory

The coupled nature of the problem, with different fluid flow regimes occurring through the intact porous solid and through cracks, and the evolution of a phase-field parameter to identify cracks, will be developed and outlined here. Throughout the presentation of the general theory the governing equations will be presented in the reference configuration. The relationships between the current and reference configurations are linked through the deformation gradient. The components of the deformation gradient, F_{iJ}, are given by,

$$F_{iJ} = \frac{\partial x_i}{\partial X_J},$$

(2.1)

where x_i are the Cartesian coordinates of a material point of the aggregate in the current state defined by the spatial domain V bounded by the surface S, and X_I are Cartesian coordinates of the same material point in the reference state corresponding to the reference domain V_0 bounded by the surface S_0. Index notation will be used throughout the presentation with summation assumed over repeated indices, lowercase indices referring to the current configuration, and uppercase indices referring to the reference configuration. The relationship between surface elements in the reference and current configurations is given by Nanson's formula as $n_i dS = J F_{Ji}^{-1} N_J dS_0$, and for volume elements is $dV = J dV_0$, where n_i and N_J are components of the unit normal to the surface in the current and reference configurations respectively, J is the determinant of the deformation gradient, and F_{Ji}^{-1} is the inverse of the deformation gradient such that $F_{Ji}^{-1} = \partial X_J / \partial x_i$.

2.1. Mass balances

First consider the conservation of mass for a fractured, fluid saturated, porous solid. Following the work of Coussy (Coussy, 1994, 1995, 2010, 1989a, 1989b) the porous solid and the fluid will together be referred to as the aggregate. In order to develop the theory within the phase-field framework we identify the total reference domain V_0, which contains both cracks and pores and is unchanging while fluid may be convected into and out of this domain.

First, the total solid mass of the system remains fixed for all time, and as such, conservation of mass for the solid can be written as,

$$\frac{D}{Dt} \int_{V_0} (1 - \phi)\rho^s J \ dV_0 = 0,$$

(2.2)

where ϕ is the reference volume fraction of porosity in the aggregate, which is assumed to always be filled by fluid, and ρ^s is the mass density of the solid. The notation D/Dt represents the time derivative with respect to an observer attached to a material point of the aggregate. Given that this equation must hold for any arbitrary region of the reference domain, the integrand must be zero pointwise, i.e.

$$\frac{D}{Dt}\left[(1-\phi)\rho^s J\right] \equiv \left[\dot{\overline{(1-\phi)\rho^s J}}\right] = 0. \tag{2.3}$$

Eq. (2.3) is the mass balance equation for the solid.

The *total* conservation of mass for the system is given by,

$$\frac{D}{Dt}\int_{V_0}\left[(1-\phi)\rho^s + \phi\rho^f\right]J\ dV_0 = -\int_{S_0}\rho^f\tilde{w}_I N_I\ dS_0 + \int_{V_0}\rho^f\tilde{m}\ dV_0, \tag{2.4}$$

where ρ^f is the mass density of the fluid, $\tilde{w}_I$ is the volume of fluid traversing a unit of reference area of the aggregate per unit of time, and $\tilde{m}$ is the fluid volume injected per unit of reference volume. Note that the nominal fluid flux $\tilde{w}_I$ is related to the true fluid flux w_i as $w_i = \tilde{w}_K F_{iK}/J$. The right-hand side of the equation represents the mass that enters the system through its surface and volume respectively.

Combining (2.2) and (2.4), the conservation of fluid mass of the system is,

$$\frac{D}{Dt}\int_{V_0}\phi\rho^f J\ dV_0 = -\int_{S_0}\rho^f\tilde{w}_I N_I dS_0 + \int_{V_0}\rho^f\tilde{m}dV_0. \tag{2.5}$$

Applying the divergence theorem, and taking (2.5) to be valid for any arbitrary volume, the point-wise form of the fluid mass balance becomes,

$$\left(\dot{\overline{\phi\rho^f J}}\right) = -\left(\rho^f\tilde{w}_I\right)_{,I} + \rho^f\tilde{m}. \tag{2.6}$$

2.2. Momentum balances

Anticipating how the equations of this theory will eventually be solved numerically, the focus of the momentum balance equations will be placed on the aggregate and then on the fluid. For the aggregate, the balance of linear momentum is written as,

$$\frac{D}{Dt}\int_{V_0}\left[(1-\phi)\rho^s v_i + \phi\rho^f\left(v_i + v_i^{f/s}\right)\right]J\ dV_0 = \int_{S_0}\tilde{t}_i\ dS_0 + \int_{V_0}\tilde{b}_i\ dV_0 - \int_{S_0}\rho^f\tilde{w}_K N_K\left(v_i + v_i^{f/s}\right)dS_0$$
$$+ \int_{V_0}\rho^f\tilde{m}\left(v_i + v_i^{f/s}\right)\ dV_0. \tag{2.7}$$

The components of the traction per unit reference area and body force per reference volume are $\tilde{t}_i$ and $\tilde{b}_i$. Note that the tractions and body forces appearing here are external to the solid/fluid aggregate. Additionally, we adopt the following ansatz that the average fluid velocity relative to the solid aggregate, $v_i^{f/s}$, is related to the true fluid flux by $w_i = \phi v_i^{f/s}$. The left-hand side of (2.7) represents the rate of change of the total momentum of the solid/fluid aggregate contained within the domain V_0. The right-hand side of the equation consists of two parts; the sum of the external forces acting on the volume, and the fluid momentum convected and injected into the volume. Note that it is assumed that the fluid injected by external sources is injected into the volume with the same velocity as the existing fluid. Next, the standard hypothesis is adopted such that the first Piola-Kirchhoff stress components, P_{ji}, are related to the nominal surface traction by,

$$\tilde{t}_i = P_{ji}N_j \text{ on } S_0 \tag{2.8}$$

The Cauchy stress is related to the first Piola-Kirchhoff stress in the normal manner as, $\sigma_{ji} = F_{jK}P_{Ki}/J$.

Application of the traction-stress relation (2.8), the divergence theorem, the mass balance Eqs. (2.3) and (2.6), and noting that the momentum balance must hold for arbitrary volumes leads to the pointwise form for Newton's second law for the aggregate,

$$P_{Ki,K} + \tilde{b}_i = (1-\phi)\rho^s J\dot{v}_i + \phi\rho^f J\left(\dot{\overline{v_i + v_i^{f/s}}}\right) + \phi\rho^f J\left(v_i + v_i^{f/s}\right)_{,K}F_{Kj}^{-1}v_j^{f/s} \tag{2.9}$$

The time derivative, $(\,\overset{\circ}{}\,)$ for an observer moving with a *fluid* particle is given by,

$$(\overset{\circ}{a}) = \dot{a} + a_{,i}v_i^{f/s} = \dot{a} + a_{,K}F_{Ki}^{-1}v_i^{f/s}. \tag{2.10}$$

Therefore, (2.9) can be re-written as,

$$P_{Ki,K} + \tilde{b}_i = (1-\phi)\rho^s J\dot{v}_i + \phi\rho^f J\left(\overset{\circ}{v_i + v_i^{f/s}}\right). \tag{2.11}$$

Next, the balance of angular momentum for the aggregate is given by,

$$\frac{D}{Dt} \int_{V_0} \epsilon_{ijk}\Big[(1 - \phi)\rho^s x_j v_k + \phi \rho^f x_j\big(v_k + v_k^{f/s} \big) \Big]J dV_0 = \int_{S_0} \epsilon_{ijk} x_j \tilde{t}_k \, dS_0 + \int_{V_0} \epsilon_{ijk} x_j \tilde{b}_k \, dV_0 - \int_{S_0} \rho^f \tilde{w}_M N_M \epsilon_{ijk} x_j\big(v_k + v_k^{f/s} \big) \, dS_0$$
$$+ \int_{V_0} \rho^f \tilde{m} \epsilon_{ijk} x_j\big(v_k + v_k^{f/s} \big) \, dV_0. \tag{2.12}$$

Here ϵ_{ijk} are the components of the permutation tensor, and x_i are the components of the position of a particle in the current configuration of the aggregate. Application of the previously established procedures yields the pointwise consequence of the angular momentum balance as,

$$\epsilon_{ijk}\big(P_{Lj} F_{kL} - J\rho^f w_j v_k - J\rho^f w_k v_j \big) = 0 \quad \rightarrow \quad P_{Ki} F_{jK} = P_{Kj} F_{iK}. \tag{2.13}$$

The implication of (2.13) is that the aggregate Cauchy stress is symmetric.

For the fluid, the linear momentum balance is,

$$\frac{D}{Dt} \int_{V_0} \phi \rho^f \big(v_i + v_i^{f/s} \big) J dV_0 = \int_{S_0} \tilde{t}_i^f dS_0 + \int_{V_0} \Big(\tilde{b}_i^{\,f} + \tilde{f}_i^{sf} \Big) dV_0 - \int_{S_0} \rho^f \tilde{w}_K N_K \big(v_i + v_i^{f/s} \big) \, dS_0$$
$$+ \int_{V_0} \rho^f \tilde{m}\big(v_i + v_i^{f/s} \big) \, dV_0. \tag{2.14}$$

Here, the components of the net traction on the fluid per unit of aggregate reference area are $\tilde{t}_i^f$, the components of the fluid body force per unit of aggregate reference volume supplied by external sources are $\tilde{b}_i^{\,f}$, and the components of the body force per unit aggregate reference volume that the solid places upon the fluid are $\tilde{f}_i^{sf}$. Here we adopt the ansatz that the fluid traction $\tilde{t}_i^f$ is related to the fluid stress by,

$$\tilde{t}_i^f = \phi T_{Ki} N_K = \phi\big(\tau_{ji} - p\delta_{ij} \big) J F_{Kj}^{-1} N_K, \tag{2.15}$$

where the components of the first Piola-Kirchhoff stress in the fluid are T_{ji}, and the Cauchy fluid stress components have been decomposed into the hydrostatic pressure p and the deviatoric part τ_{ij}. Here we have introduced the Kronecker delta components δ_{ij}. Again, notice that fluid momentum is convected and injected into the volume of the aggregate being considered. Analysis of (2.14) using the previously discussed procedures along with (2.10) and (2.15) gives the pointwise form for Newton's second law for the fluid,

$$\big(\phi T_{ji} \big)_{,J} + \tilde{b}_i^{\,f} + \tilde{f}_i^{sf} = \phi \rho^f J \big(\mathring{v}_i + \mathring{v}_i^{f/s} \big) \tag{2.16}$$

The balance of angular momentum for the fluid is,

$$\frac{D}{Dt} \int_{V_0} \epsilon_{ijk} \phi \rho^f x_j \big(v_k + v_k^{f/s} \big) J dV_0 = \int_{S_0} \epsilon_{ijk} x_j \tilde{t}_k^f \, dS_0 + \int_{V_0} \epsilon_{ijk} x_j \Big(\tilde{b}_k^{\,f} + \tilde{f}_k^{sf} \Big) dV_0 - \int_{S_0} \rho^f \tilde{w}_M N_M \epsilon_{ijk} x_j \big(v_k + v_k^{f/s} \big) \, dS_0$$
$$+ \int_{V_0} \rho^f \tilde{m} \epsilon_{ijk} x_j \big(v_k + v_k^{f/s} \big) \, dV_0. \tag{2.17}$$

The analysis of this integral form provides the pointwise form of angular fluid momentum,

$$\epsilon_{ijk}\big(\phi T_{Lj} F_{kL} - J\rho^f w_j v_k - J\rho^f w_k v_j \big) = 0 \quad \rightarrow \quad T_{Li} F_{jL} = T_{Lj} F_{iL}. \tag{2.18}$$

We note that (2.11) and (2.16), along with the relationship for the fluid force on the solid per unit aggregate volume, $\tilde{f}_i^{fs} = -\tilde{f}_i^{sf}$, can be used to derive Newton's second law for the solid as,

$$\big(P_{ji} - \phi T_{ji} \big)_{,J} + \underbrace{\tilde{b}_i - \tilde{b}_i^{\,f}}_{\tilde{b}_i^{\,s}} - \tilde{f}_i^{sf} = (1 - \phi) J\rho^s \mathring{v}_i. \tag{2.19}$$

Here we have introduced the definition of the external body force acting on the solid per unit aggregate volume $\tilde{b}_i^{\,s}$.

2.3. Micro-forces and their balance

Within this theory the material is allowed to fail or damage according to the phase-field theory of fracture for brittle solids. Using the phase-field damage parameter, following the approach of Fried, Gurtin, and others (Fried and Gurtin, 1993, 1994; Wilson et al., 2013), we need also to introduce a set of conjugate forces associated with changes in this quantity. To this end, we define $\tilde{\tau}$ as an external surface micro-force such that $\tilde{\tau}\dot{\mu}$ is the power expended per unit area of aggregate surface by sources external to the volume under consideration, $\tilde{\gamma}$ is an external body micro-force such that $\tilde{\gamma}\dot{\mu}$ is the power expended per unit aggregate volume by external sources, and $\tilde{\pi}$ is an internal micro-force per unit aggregate volume such that $\tilde{\pi}\dot{\mu}$ is the power expended internally on the material per unit volume (Gurtin, 1996). We also assume that on the surface there is a balance between the applied surface micro-force $\tilde{\tau}$ and the material micro-force vector $\tilde{\xi}_i$ such that,

$$\tilde{t} = \tilde{\xi}_J N_J \text{ on } S_0. \tag{2.20}$$

It is then also assumed that there exists a net balance of this set of micro-forces such that,

$$\int_{S_0} \tilde{t} \, dS_0 + \int_{V_0} \tilde{\gamma} \, dV_0 + \int_{V_0} \tilde{\pi} \, dV_0 = 0. \tag{2.21}$$

Application of the divergence theorem, (2.20), and the argument that the micro-force balance must hold for any arbitrary volume yields the pointwise micro-force balance equation,

$$\tilde{\xi}_{I,I} + \tilde{\gamma} + \tilde{\pi} = 0. \tag{2.22}$$

2.4. Energy balances

Next, consider the balance of energy in the solid/fluid aggregate. The integral form for the first law of thermodynamics for a given aggregate volume is written as,

$$
\begin{aligned}
\frac{D}{Dt} & \int_{V_0} \left[\tfrac{1}{2}(1 - \phi)\rho^s v_i \, v_i + (1 - \phi)\rho^s e^s \right] dV_0 + \frac{D}{Dt} \int_{V_0} \left[\tfrac{1}{2}\phi\rho^f \left(v_i + v_i^{f/s} \right)\left(v_i + v_i^{f/s} \right) + \tfrac{1}{2}\phi\rho^f A v_i^{f/s} v_i^{f/s} + \phi\rho^f e^f \right] dV_0 \\
& = \int_{S_0} \tilde{t}_i v_i \, dS_0 + \int_{V_0} \left[\tilde{b}_i v_i + \tilde{b}_i^f v_i^{f/s} \right] dV_0 + \int_{S_0} \tilde{t}_i^f v_i^{f/s} \, dS_0 + \int_{V_0} \tilde{m} p \, dV_0 \\
& \quad + \int_{S_0} \tilde{t}\dot{\mu} \, dS_0 + \int_{V_0} \tilde{\gamma}\dot{\mu} \, dV_0 - \int_{S_0} \tilde{q}_J N_J \, dS_0 + \int_{V_0} \tilde{r} \, dV_0 \\
& \quad - \int_{S_0} \rho^f \tilde{w}_K N_K \left[\tfrac{1}{2}\left(v_i + v_i^{f/s} \right)\left(v_i + v_i^{f/s} \right) + \tfrac{1}{2}A v_i^{f/s} v_i^{f/s} + e^f \right] dS_0 \\
& \quad + \int_{V_0} \rho^f \tilde{m} \left[\tfrac{1}{2}\left(v_i + v_i^{f/s} \right)\left(v_i + v_i^{f/s} \right) + \tfrac{1}{2}A v_i^{f/s} v_i^{f/s} + e^f \right] dV_0.
\end{aligned}
\tag{2.23}
$$

Again, notice that the definitions of the body forces are in terms of the forces per unit aggregate reference volume such that the total body force $\tilde{b}_i$ is simply the sum of the external body force per unit aggregate volume on the fluid $\tilde{b}_i^f$ and the external body force per unit aggregate volume on the solid $\tilde{b}_i^s$. Also appearing in the energy balances are the volumetric sources of heat $\tilde{r}$ supplied per unit reference volume of the aggregate per unit of time. Note that the total heat supply to the aggregate $\tilde{r}$ includes heat supplied both to the solid and to the fluid, which is partitioned as $\tilde{r} = \tilde{r}^s + \tilde{r}^f$. Then, $\tilde{q}_J$ are the components of the net heat flux traversing a unit reference area of the aggregate per unit of time. Likewise, the total heat flux $\tilde{q}_I$ represents contributions from the solid and the fluid such that it can be partitioned into contributions per unit aggregate reference area as $\tilde{q}_I = \tilde{q}_I^s + \tilde{q}_I^f$. The additional freshly introduced quantities are the internal energy per unit mass of solid e^s, the internal energy per unit mass of fluid e^f, and the tortuosity A.

The left-hand side of this energy balance equation contains the time rate of change of the kinetic and internal energy contained within a region of the solid/fluid aggregate. Aside from the term containing the tortuosity, each of these terms is conventional, with the kinetic and internal energies of the solid and fluid partitioned through the porosity. The additional term $\tfrac{1}{2}\phi\rho^f A v_i^{f/s} v_i^{f/s}$ accounts for the kinetic energy of the fluid per unit aggregate volume that is omitted by the term $\tfrac{1}{2}\phi\rho^f \left(v_i + v_i^{f/s} \right)\left(v_i + v_i^{f/s} \right)$. Since $\left(v_i + v_i^{f/s} \right)$ is the average velocity of the fluid, it is valid to claim that the integral of the average velocity is equivalent to the integral of the velocity, however such a relationship does not hold for the square of the velocity and the square of the average velocity. Hence, it is common to introduce the tortuosity to account for this discrepancy. Note that the form for the kinetic energy correction $\tfrac{1}{2}\phi\rho^f A v_i^{f/s} v_i^{f/s}$ assumes that the fluctuation of the total fluid velocity about its average value is proportional to the average relative velocity of the fluid with respect to the solid, $v_i^{f/s}$. In general, the tortuosity A will depend upon the specific structure of the porosity, the porosity itself, and the relative fluid velocity $v_i^{f/s}$ (Coussy, 1994).

The first line of the right-hand side of this energy balance equation includes the power expended by the total traction on the aggregate surface, the power expended by the external body forces on the solid and fluid accounted for separately, the power expended by the fluid stress on the relative velocity at the surface (the power expended by the fluid stress on the aggregate velocity v_i is included in the work done by the total traction), and the power expended by external sources to inject additional fluid volume into the aggregate. The second line of the right-hand side includes the power expended by external micro-forces on the surface and in the volume of the aggregate, and the rate of heat supplied to the aggregate volume across its surface and to the volume directly. Note that since it is an *internal* force, the internal micro-force $\tilde{\pi}$ does not enter the energy balance equation. This is analogous to the fact that the internal force that the solid places upon the fluid, $\tilde{f}_i^{sf}$, does not enter this energy balance equation either. Finally, the last two lines of the right-hand side represent the energy convected into the volume through its surface, and injected into the volume directly. Note that these terms contain both kinetic and stored energy contributions from the fluid, and it is assumed that the fluid injected directly into the volume arrives with the prevailing kinetic and internal energy of the existing fluid.

The analysis of the energy balance equation requires the use of the mass balances (2.3) and (2.6), the momentum balances (2.11) and (2.16), and the micro-force balance (2.22), leading to the following pointwise form for the first law for the solid/fluid aggregate,

$$
(1 - \phi)J\rho^s \dot{e}^s + \phi J\rho^f \overset{\circ}{e}{}^f + \phi J\rho^f \left(\frac{1}{2} A v_i^{f/s} v_i^{f/s} \right) = \left(P_{Ji} - \phi \tilde{\tau}_{Ji} \right) v_{i,J} + \phi \tilde{\tau}_{Ji} \left(v_i + v_i^{f/s} \right)_{,J} + p(\dot{\phi J}) \ + \left[p \left(\phi J F_{Ji}^{-1} \right)_{,J} - \tilde{f}_i^{sf} \right] v_i^{f/s}
$$

$$
+ \, \xi_I \dot{\mu}_{,I} - \tilde{\pi}\dot{\mu} + \phi p J \frac{\overset{\circ}{\rho}{}^f}{\rho^f} - \tilde{q}_{I,I} + \tilde{r}. \tag{2.24}
$$

Here we have introduced the first Piola-Kirchhoff stress in the fluid associated with the deviatoric part of the fluid stress τ_{ji}, $\tilde{\tau}_{Ji} = J F_{Jk}^{-1} \tau_{ki}$.

It is also useful to analyze the energy balances for the solid and fluid separately, noting that the sum of the solid and fluid energies must equate to the solid/fluid aggregate energy. For the solid, the first law energy balance is,

$$
\frac{D}{Dt} \int_{V_0} \left[\frac{1}{2} (1 - \phi) \rho^s v_i \, v_i + (1 - \phi) \rho^s e^s \right] J dV_0 = \int_{S_0} \left(\tilde{t}_i - \tilde{t}_i^f \right) v_i \, dS_0 + \int_{V_0} \tilde{b}_i^{\,s} v_i dV_0 + \int_{S_0} \tilde{\tau}\mu \, dS_0 + \int_{V_0} \tilde{\gamma}\mu dV_0
$$

$$
- \int_{S_0} \tilde{q}_j^s N_j \, dS_0 + \int_{V_0} \left(\tilde{r}^s + \tilde{r}^{fs} \right) dV_0 + \int_{V_0} \tilde{\varpi}^{fs} dV_0. \tag{2.25}
$$

Note, that as for the body forces, the surface traction can be decomposed into its solid and fluid contributions per unit aggregate reference area. In (2.25) the traction associated with the solid is $\tilde{t}_i^s = \tilde{t}_i - \tilde{t}_i^f$. The mechanical power density that the fluid transfers to the solid per unit of time is $\tilde{\varpi}^{fs}$, and the thermal power density that the fluid transfers to the solid per unit of time is r^{fs}. The mechanical power per reference volume that the solid transfers to the fluid, $\tilde{\varpi}^{sf}$, the force that the solid imparts upon the fluid, $\tilde{f}_i^{sf}$, and the heat that the solid transfers to the fluid, $\tilde{r}^{sf}$, are each the opposites of those from the fluid to the solid. The mechanical power density that the fluid transfers to the solid, $\tilde{\varpi}^{fs}$, consists of the dot product of the force density of the fluid on the solid with the solid velocity and the fluid pressure working to open up additional porosity. Hence, the power term $\tilde{\varpi}^{fs}$ is given by,

$$
\tilde{\varpi}^{fs} = \tilde{f}_i^{fs} v_i + p J \dot{\phi}. \tag{2.26}
$$

The pointwise form for the first law for the solid obtained from the analysis of (2.25), (2.3), (2.19), (2.22), and (2.26) is,

$$
(1 - \phi)J\rho^s \dot{e}^s = \left(P_{Ji} - \phi\tilde{\tau}_{Ji} \right) v_{i,J} + p(\dot{\phi J}) \ + \xi_I \dot{\mu}_{,I} - \tilde{q}_{I,I}^s + \tilde{r}^s - \tilde{r}^{sf} - \tilde{\pi}\dot{\mu}. \tag{2.27}
$$

Adopting the following stress partition, the solid stress P_{Ji}^s is defined as,

$$
(1 - \phi)P_{Ji}^s = P_{Ji} - \phi T_{Ji} , \tag{2.28}
$$

and (2.27) can be rewritten as,

$$
(1 - \phi)J\rho^s \dot{e}^s = \left[(1 - \phi)P_{Ji}^s - \phi J F_{Ji}^{-1} p \right] v_{i,J} + p(\dot{\phi J}) \ - \tilde{\pi}\dot{\mu} + \xi_I \dot{\mu}_{,I} - \tilde{q}_{I,I}^s + \tilde{r}^s - \tilde{r}^{sf}. \tag{2.29}
$$

Then, the first law energy balance for the fluid is simply the difference between the aggregate energy balance and the solid energy balance.

$$
\phi J\rho^f \overset{\circ}{e}{}^f + \phi J\rho^f \left(\frac{1}{2} A v_i^{f/s} v_i^{f/s} \right) = \phi J p \frac{\overset{\circ}{\rho}{}^f}{\rho^f} + \phi \tilde{\tau}_{Ji} \left(v_i + v_i^{f/s} \right)_{,J} - \tilde{q}_{I,I}^f + \tilde{r}^f + \tilde{r}^{sf} + \left[p \left(\phi J F_{Ji}^{-1} \right)_{,J} - \tilde{f}_i^{sf} \right] v_i^{f/s}. \tag{2.30}
$$

2.5. Entropy inequalities

In this section the entropy inequalities arising from the second law of thermodynamics for the solid, fluid, and solid/fluid aggregate are analyzed. First, consider the continuum form for the second law of thermodynamics for the solid,

$$
\frac{D}{Dt} \int_{V_0} (1 - \phi) \rho^s s^s J dV_0 \geq - \int_{S_0} \frac{\tilde{q}_j^s N_j}{\theta^s} \, dS_0 + \int_{V_0} \frac{\tilde{r}^s - \tilde{r}^{sf}}{\theta^s} dV_0. \tag{2.31}
$$

Here, the left-hand side of the inequality is the rate of change of the entropy in the solid, and the right-hand side represents the entropy transfer to the solid. Next, we introduce the Helmholtz free energy per unit mass for the solid as,

$$
\psi^s = e^s - s^s \theta^s. \tag{2.32}
$$

Application of (2.3), (2.27), and (2.32) yields the pointwise form for the entropy inequality for the solid as,

$$\left(1 - \phi\right)J\rho^s\psi^s \leq \left[\left(1 - \phi\right)P^s_{ji} - \phi JF^{-1}_{ji}p\right]v_{i,J} + p(\dot{\phi J}) - \tilde{\pi}\dot{\mu} + \xi_I\dot{\mu}_I - \left(1 - \phi\right)J\rho^s s^s\dot{\theta}^s - \frac{1}{\theta^s}\tilde{q}^s_I\theta^s_{,I}.$$ (2.33)

We now assume that the Helmholtz free energy of the solid ψ^s, the solid stress P^s_{ji}, the internal micro-force vector ξ_I, the internal micro force $\tilde{\pi}$, the solid entropy density s^s, and the heat flux in the solid $\tilde{q}^s_I$, each can depend upon the temperature in the solid θ^s, its gradient $\theta^s_{,I}$, the true porosity ϕJ, the phase-field variable μ, its gradient μ_I, its rate $\dot{\mu}$, and the deformation gradient F_{iJ}. The velocity gradient is related to the material time derivative of the deformation gradient as, $\dot{F}_{iK} = F_{jK}v_{i,j}$. Eq. (2.33) becomes,

$$0 \geq \left[\left(1 - \phi\right)J\rho^s\frac{\partial\psi^s}{\partial F_{iJ}} - \left(1 - \phi\right)P^s_{ji} + \phi JF^{-1}_{ji}p\right]v_{i,J} + \left[\left(1 - \phi\right)J\rho^s\frac{\partial\psi^s}{\partial\mu_I} - \xi_I\right]\dot{\mu}_I + \left[\left(1 - \phi\right)J\rho^s\frac{\partial\psi^s}{\partial\mu} + \tilde{\pi}\right]\dot{\mu}$$
$$+ \left[\left(1 - \phi\right)J\rho^s\frac{\partial\psi^s}{\partial\dot{\mu}}\right]\ddot{\mu} + \left[\left(1 - \phi\right)J\rho^s\frac{\partial\psi^s}{\partial(\phi J)} - p\right](\dot{\phi J}) + \left(1 - \phi\right)J\rho^s\left[\frac{\partial\psi^s}{\partial\theta^s} + s^s\right]\dot{\theta}^s + \left[\left(1 - \phi\right)J\rho^s\frac{\partial\psi^s}{\partial\theta^s_{,I}}\right]\dot{\theta}^s_{,I} + \frac{1}{\theta^s}\tilde{q}^s_I\theta^s_{,I}. \quad (2.34)$$

Following the procedures of Coleman and Noll (1963), Eq. (2.34) must hold for all admissible processes associated with arbitrary variations of $v_{i,j}$, $\dot{\mu}_I$, $\dot{\mu}$, $\ddot{\mu}$, $(\dot{\phi J})$, $\dot{\theta}^s$, and $\dot{\theta}^s_{,I}$. The inequality is linear in $v_{i,j}$, $\dot{\mu}_I$, $\ddot{\mu}$, $(\dot{\phi J})$, $\dot{\theta}^s$, and $\dot{\theta}^s_{,I}$, which implies that the coefficients contracted with these terms must be zero in order for the inequality to hold for all admissible processes, leading to the following constitutive equations for the solid,

$$\left(1 - \phi\right)P^s_{ji} = \left(1 - \phi_0\right)J_0\rho^s_0\frac{\partial\psi^s}{\partial F_{iJ}} + \phi JF^{-1}_{ji}p$$

$$\xi_I = \left(1 - \phi_0\right)J_0\rho^s_0\frac{\partial\psi^s}{\partial\mu_I}$$

$$p = \left(1 - \phi_0\right)J_0\rho^s_0\frac{\partial\psi^s}{\partial(\phi J)}$$

$$s^s = -\frac{\partial\psi^s}{\partial\theta^s}$$

$$\frac{\partial\psi^s}{\partial\dot{\mu}} = \frac{\partial\psi^s}{\partial\theta^s_{,I}} = 0 . \quad (2.35)$$

Notice that for the reference configuration relationships we have used the fact that $(1 - \phi)\rho^s J = (1 - \phi_0)\rho^s_0 J_0$ from (2.3), where the subscript "0" refers to the values of the quantities in the reference state. The reduced form of the dissipation inequality for the solid is then,

$$\left[\left(1 - \phi\right)J\rho^s\frac{\partial\psi^s}{\partial\mu} + \tilde{\pi}\right]\dot{\mu} + \frac{1}{\theta^s}\tilde{q}^s_I\theta^s_{,I} \leq 0 \quad (2.36)$$

This reduced dissipation inequality is satisfied if,

$$\tilde{\pi} = -\left(1 - \phi_0\right)J_0\rho^s_0\frac{\partial\psi^s}{\partial\mu} - \beta\dot{\mu} - \eta_I\theta^s_{,I}$$

$$\tilde{q}^s_I = -\bar{\eta}_I\dot{\mu} - \kappa^s_{IJ}\theta^s_{,J}, \quad (2.37)$$

with the positivity condition,

$$\beta\dot{\mu}^2 + \dot{\mu}\eta_I\theta^s_{,I} + \theta^s_{,I}\bar{\eta}_I\dot{\mu} + \theta^s_{,I}\kappa^s_{IJ}\theta^s_{,J} \geq 0 \quad \text{for all } \dot{\mu}, \theta^s_{,I} \quad (2.38)$$

Each of the newly introduced material properties, β, η_I, $\bar{\eta}_I$, and κ^s_{IJ} are allowed to depend upon μ_I, μ, $\dot{\mu}$, (ϕJ), θ^s, $\theta^s_{,I}$, and F_{iJ}. Note that κ^s_{IJ} is the thermal conductivity tensor for the solid skeleton.

We now consider the fluid. For the fluid, the second law inequality is,

$$\frac{D}{Dt}\int_{V_0}\phi\rho^f s^f J dV_0 \geq -\int_{S_0}\frac{\tilde{q}^f_J N_J}{\theta^f}\,dS_0 + \int_{V_0}\frac{\tilde{r}^f + \tilde{r}^{sf}}{\theta^f}dV_0 - \int_{S_0}\rho^f\tilde{w}_J N_J s^f\,dS_0 + \int_{V_0}\rho^f\tilde{m}s^f dV_0. \quad (2.39)$$

Here, the left-hand side of the inequality is the rate of change of the entropy in the fluid, and the right-hand side represents the entropy transfer to the fluid including the entropy of the convected and injected fluid. The Helmholtz free energy for the fluid is,

$$\psi^f = e^f - s^f\theta^f \quad (2.40)$$

Application of (2.6), (2.30), and (2.40) leads to the pointwise form for the second law inequality for the fluid as,

$$\phi J \rho^f \psi^f \leq \phi J p \frac{\mathring{\rho}^f}{\rho^f} - \phi J \rho^f s^f \mathring{\theta}^f + \phi \tilde{\tau}_{ji} \left(v_i + v_i^{f/s} \right)_{,J} - \phi J \rho^f \left[\frac{1}{2} A \mathring{v}_i^{f/s} + A \left(\mathring{v}_i^{f/s} \right) \right] v_i^{f/s}$$

$$+ \left[p \left(\phi J F_{ji}^{-1} \right)_{,J} - \tilde{f}_i^{sf} \right] v_i^{f/s} - \frac{1}{\theta^f} \tilde{q}_i^f \theta_{,i}^f. \tag{2.41}$$

In contrast to the analysis of the second law for the solid, here we do not invoke the principle of equipresence, i.e. that each dependent quantity depends upon each of the independent quantities. Instead, we take a slightly more restrictive set of assumptions for the analysis of (2.41). We assume that the Helmholtz free energy of the fluid ψ^f, the fluid pressure p, and the entropy density of the fluid s^f are dependent only on the density of the fluid ρ^f, the fluid velocity gradient $v_{i,J}^f = v_{i,J} + v_{i,J}^{f/s}$, the temperature of the fluid θ^f, and the temperature gradient in the fluid $\theta_{,I}^f$. The remaining dependent quantities, include the fluid stress $\tilde{\tau}_{ji}$, the heat flux in the fluid $\tilde{q}_i^f$, and the interaction force between the solid and fluid $\tilde{f}_i^{sf}$, each of which can depend upon $\rho^f, \theta^f, \theta_{,I}^f, \phi, v_{i,J}^f$, as well as the relative fluid velocity $v_i^{f/s}$, its rate with respect to the fluid $\left(\mathring{v}_i^{f/s} \right)$, the deformation gradient F_{iJ}, and the phase-field parameter μ. Eq. (2.41) then becomes,

$$0 \geq \phi J \left[\rho^f \frac{\partial \psi^f}{\partial \rho^f} - \frac{p}{\rho^f} \right] \mathring{\rho}^f + \phi J \rho^f \left[\frac{\partial \psi^f}{\partial \theta^f} + s^f \right] \mathring{\theta}^f + \phi J \rho^f \frac{\partial \psi^f}{\partial \theta_{,I}^f} \mathring{\theta}_{,I}^f + \phi J \rho^f \frac{\partial \psi^f}{\partial v_{i,J}^f} \left(\mathring{v}_{i,J}^f \right) + \phi J \rho^f \left[\frac{1}{2} A \mathring{v}_i^{f/s} + A \left(\mathring{v}_i^{f/s} \right) \right] v_i^{f/s}$$

$$- \left[p \left(\phi J F_{ji}^{-1} \right)_{,J} - \tilde{f}_i^{sf} \right] v_i^{f/s} + \frac{1}{\theta^f} \tilde{q}_i^f \theta_{,I}^f - \phi \tilde{\tau}_{ji} v_{i,J}^f \tag{2.42}$$

Eq. (2.42) must hold for all admissible processes associated with arbitrary variations of $\mathring{\rho}^f, \mathring{\theta}^f, \mathring{\theta}_{,I}^f, \mathring{v}_{i,J}^f, \left(\mathring{v}_{i,J}^f \right), v_i^{f/s}$, and $\left(\mathring{v}_i^{f/s} \right)$. The inequality is linear in $\mathring{\rho}^f, \mathring{\theta}^f, \left(\mathring{v}_{i,J}^f \right)$, and $\mathring{\theta}_{,I}^f$, which implies that the coefficients contracted with these terms must be zero in order for the inequality to hold for all admissible processes, leading to the constitutive equations for the fluid,

$$p = \left(\rho^f \right)^2 \frac{\partial \psi^f}{\partial \rho^f}$$

$$s^f = - \frac{\partial \psi^f}{\partial \theta^s}$$

$$\frac{\partial \psi^f}{\partial \theta_{,I}^f} = 0, \quad \frac{\partial \psi^f}{\partial v_{i,J}^f} = 0, \tag{2.43}$$

and the reduced dissipation inequality for the fluid,

$$\left[\phi J \rho^f \left(\frac{1}{2} A \mathring{v}_i^{f/s} + A \left(\mathring{v}_i^{f/s} \right) \right) - p \left(\phi J F_{ji}^{-1} \right)_{,J} + \phi_J \tilde{\tau}_{ji} + \tilde{f}_i^{sf} \right] v_i^{f/s} - \tilde{\tau}_{ji} \left(w_{i,J} + \phi v_{i,J} \right) + \frac{1}{\theta^f} \tilde{q}_i^f \theta_{,I}^f \leq 0. \tag{2.44}$$

This reduced dissipation inequality for the fluid is satisfied if,

$$\tilde{\tau}_{ji} = \nu_{ijkL} \left(w_{k,L} + \phi v_{k,L} \right) + \hat{\tau}_{ji}$$

$$\tilde{q}_i^f = - \kappa_{ij}^f \theta_{,J}^f + \hat{q}_I$$

$$\tilde{f}_i^{sf} = - \chi_{ij} v_i^{f/s} - \phi_J \tilde{\tau}_{ji} + p \left(\phi J F_{ji}^{-1} \right)_{,J} - \phi J \rho^f \left(\frac{1}{2} A \mathring{v}_i^{f/s} - A \left(\mathring{v}_i^{f/s} \right) \right) + \hat{f}_i^{sf} \tag{2.45}$$

Here we have focused on the direct terms for the deviatoric fluid stress, the fluid heat flux, and the solid/fluid interaction force introducing the positive definite material tensors of the fluid viscosity ν_{ijkL}, the thermal conductivity of the fluid κ_{ij}^f, and the fluid impermeability of the porous solid χ_{ij}. Each of these material tensors is allowed to depend upon $\rho^f, \theta^f, \theta_{,I}^f, \phi, v_{i,J}^f, v_i^{f/s}$, and $\left(\mathring{v}_i^{f/s} \right), F_{iJ}$, and μ. The additional functions $\hat{\tau}_{ji}, \hat{q}_i$, and $\hat{f}_i^{sf}$ are not written out explicitly for the sake of brevity, but their general construction and positivity constraint is analogous to that spelled out for the solid in (2.37) and (2.38). In practice, each of these functions will usually be taken to vanish, as will the cross terms in (2.37).

At this point there remains one quantity that has not been constrained, the heat transferred from the solid to the fluid, $\tilde{r}^{sf} = - \tilde{r}^{fs}$. For this we consider the second law inequality for the solid/fluid aggregate as a whole,

$$\frac{D}{Dt} \int_{V_0} \left[(1 - \phi)\rho^s s^s + \phi\rho^f s^f \right] J dV_0 \geq - \int_{S_0} \frac{\tilde{q}_J^s N_J}{\theta^s} + \frac{\tilde{q}_J^f N_J}{\theta^f} dS_0 + \int_{V_0} \left(\frac{\tilde{r}^s + \tilde{r}^{fs}}{\theta^s} + \frac{\tilde{r}^f + \tilde{r}^{sf}}{\theta^f} \right) dV_0 - \int_{S_0} \rho^f \tilde{w}_J N_J s^f dS_0$$
$$+ \int_{V_0} \rho^f \tilde{m} s^f dV_0. \tag{2.46}$$

Here, the left-hand side of the inequality is the rate of change of the entropy in the aggregate, and the right-hand side represents the entropy transfer to the aggregate including entropy convected and injected into the aggregate by the fluid. Applying the previously derived constitutive equations, the pointwise form is,

$$0 \leq \frac{1}{\theta^f} \left\{ \phi \tilde{\tau}_{ji} v_{i,J}^f - \phi J\rho^f \left[\frac{1}{2} \mathring{A} v_i^{f/s} + A \left(\mathring{v}_i^{f/s} \right) \right] v_i^{f/s} + \left[p \left(J\phi F_{Ji}^{-1} \right)_{,J} - \tilde{f}_i^{sf} \right] v_i^{f/s} - \frac{1}{\theta^f} \tilde{q}_i^f \theta_{,i}^f \right\}$$
$$+ \frac{1}{\theta^s} \left\{ \left[(1 - \phi)J\rho^s \frac{\partial \psi^s}{\partial \mu} + \tilde{\pi} \right] \dot{\mu} - \frac{1}{\theta^s} \tilde{q}_i^s \theta_{,i}^s \right\} + \frac{\tilde{r}^{sf} \left(\theta^s - \theta^f \right)}{\theta^s \theta^f}. \tag{2.47}$$

The two terms in brackets have already appeared in the dissipation inequalities for the fluid (2.44) and solid (2.36) and each is already constrained to be non-negative. Hence, (2.47) still does not offer a clear constraint upon the heat transferred between the solid and fluid. However, a reasonable approach is to take the interpretation that each of the components of (2.47) must satisfy the inequality independently of the others. Then, the third term will satisfy the inequality if,

$$\tilde{r}^{sf} = \tilde{h}^{sf} \left(\theta^s - \theta^f \right). \tag{2.48}$$

Here, $\tilde{h}^{sf}$ is an effective heat transfer coefficient for the porous solid/fluid system, which must be positive and can depend upon each of the independent variables associated with the fluid and the solid.

2.6. The solid free energy

At this point the model is relatively general and has many material properties that must be specified. In this section a free energy potential is devised that simultaneously models the linear poroelasticity of Biot-type models and the onset and propagation of fluid filled fractures within the medium. Toward this end a "poro-enthalpy" potential Ω^s is proposed that can be derived from the Hemholtz free energy by the following Legendre transformation,

$$(1 - \phi_0)J_0 \rho_0^s \Omega^s = (1 - \phi_0)J_0 \rho_0^s \psi^s - Jp\phi. \tag{2.49}$$

Then, the entropy inequality for the solid (2.33) can be rewritten as,

$$(1 - \phi)J\rho^s \dot{\Omega}^s \leq \left[(1 - \phi)P_{Ji}^s - \phi pJF_{Ji}^{-1} \right] v_{i,J} - \phi J \dot{p} - \tilde{\pi}\dot{\mu} + \xi_I \dot{\mu}_I - (1 - \phi)J\rho^s s^s \dot{\theta}^s - \frac{1}{\theta^s} \tilde{q}_i^s \theta_{,i}^s, \tag{2.50}$$

and the constitutive relations outlined by (2.35) and (2.37) can be written in terms of Ω^s as,

$$(1 - \phi)P_{Ji}^s = (1 - \phi_0)J_0 \rho_0^s \frac{\partial \Omega^s}{\partial F_{iJ}} + \phi pJF_{Ji}^{-1}$$

$$\xi_I = (1 - \phi_0)J_0 \rho_0^s \frac{\partial \Omega^s}{\partial \mu_I}$$

$$\phi J = - (1 - \phi_0)J_0 \rho_0^s \frac{\partial \Omega^s}{\partial p}$$

$$s^s = - \frac{\partial \Omega^s}{\partial \theta^s}$$

$$\frac{\partial \Omega^s}{\partial \dot{\mu}} = \frac{\partial \Omega^s}{\partial \theta_{,i}^s} = 0$$

$$\tilde{\pi} = - (1 - \phi_0)J_0 \rho_0^s \frac{\partial \Omega^s}{\partial \mu} - \beta\dot{\mu} - \eta_I \theta_{,i}^s$$

$$\tilde{q}_i^s = - \bar{\eta}_I \dot{\mu} - \kappa_{ij}^s \theta_{,j}^s. \tag{2.51}$$

We consider the following simple poro-enthalpy for reversible, hyperelastic, isothermal behavior,

$$(1 - \phi_0)J_0 \rho_0^s \Omega^s = g_d(\mu)\Omega^+(F_{iJ}) + \Omega^-(F_{iJ}) - \left[\alpha + (1 - \alpha)g_m(\mu) \right] (J - 1)p$$
$$- \left[1 - g_m(\mu) \right] \frac{p^2}{2N} - \phi_0 p + \frac{G_c}{4\ell_0} \left[(1 - \mu)^2 + 4\ell_0^2 \mu_{,I} \mu_{,I} \right]. \tag{2.52}$$

Here an additive decomposition of the elastic strain-energy $\Omega^{\mathrm{el}} = \Omega^+ + \Omega^-$ has been employed so degradation is driven by the presence of tensile deformations. The material constants α, N, and G_c are a coupling coefficient commonly referred to as the Biot coefficient, the Biot tangent modulus, and Griffith's critical energy release rate, respectively, and ϕ_0 is the intrinsic porosity. Note that we invoke the compatibility relations described in (Coussy, 1994, pp. 79) to relate the Biot coefficient, the intrinsic porosity ϕ_0, and Biot's tangent modulus such that,

$$\frac{1}{N} = \frac{(\alpha - \phi_0)(1 - \alpha)}{K},\tag{2.53}$$

where K is the bulk modulus of the aggregate.

The last term in (2.52) is ubiquitous to the second order theory for phase-field fracture theories as originally proposed by Francfort and Marigo (1998) in their pioneering work on the variational approach to fracture, where ℓ_0 is a nonlinear process zone length scale. The degradation function $g_d(\mu)$ is left in general terms for the sake of simplicity. In practice, the "bell-curve" formulation employed by Wilson et al. (2013) will be used,

$$g_d(\mu) = a\left[1 - \left(\frac{a-1}{a}\right)^{\mu^2}\right]\tag{2.54}$$

with $a > 1$. The above function necessarily satisfies the properties required for degrading energy in the solid as described by Miehe et al. (2010), namely,

$$g_d(0) = 0, \quad g_d(1) = 1, \quad g_d^{'}(0) = 0.\tag{2.55}$$

The parameter a is typically chosen to be close to 1, in which case (2.54) has several advantages when compared to the more conventional $g_d(\mu) = \mu^2$. Most notably, from a simple analysis of uniaxial, homogenous behavior, the stress and phase-field μ in the solid approach zero more quickly for large values of strain that exceed the critical value for the onset of degradation. This property is particularly useful for materials with very low permeabilities, which, typically, are the materials that are candidates for hydraulic fracture treatments. Similar treatments of the degradation of the strain energy are discussed in Miehe et al., 2015. For more details of the advantages of (2.54) the reader is directed to the aforementioned work by Wilson et al. (2013).

Finally, the form of the function $g_m(\mu)$ in (2.52) is chosen such that $g_m(0) = 1$, $g_m^{'}(0) = 0$, $g_m(1) = 0$, $g_m^{'}(1) = 0$ and $0 \leq g_m(\mu) \leq 1$ in order to cause the porosity to approach unity within open cracks, as will be discussed in more detail shortly.

A simple function that satisfies these requirements is,

$$g_m(\mu) \equiv \begin{cases} 1 & ; \quad \mu < 0 \\ 1 - 3\mu^2 + 2\mu^3 & ; \quad 0 \leq \mu \leq 1, \\ 0 & ; \quad \mu > 1 \end{cases}\tag{2.56}$$

and will be adopted in this work.

For additional clarity, the constitutive relations of (2.51) can be written explicitly using the poro-enthalpy potential (2.52), $\beta = 0$, and $\eta_I = 0$ as,

$$(1 - \phi)P_{ji}^s = g_d(\mu)\frac{\partial \Omega^+}{\partial F_{iJ}} + \frac{\partial \Omega^-}{\partial F_{iJ}} + \left[\phi - \alpha - g_m(\mu)(1 - \alpha)\right]JF_{Ji}^{-1}p$$

$$\phi J = \phi_0 + \left[\alpha + g_m(\mu)(1 - \alpha)\right](J - 1) + \left[1 - g_m(\mu)\right]\frac{p}{N}$$

$$\bar{\pi} = -g_d^{'}(\mu)\Omega^+(F_{iJ}) + \frac{G_c}{2\ell_0}(1 - \mu) + g_m^{'}(\mu)\left[(1 - \alpha)(J - 1)p - \frac{1}{2N}p^2\right]$$

$$\bar{\xi}_I = 2G_c\ell_0\mu_I.\tag{2.57}$$

Using (2.28) the total aggregate stress is,

$$P_{Ji} = g_d(\mu)\frac{\partial \Omega^+}{\partial F_{iJ}} + \frac{\partial \Omega^-}{\partial F_{iJ}} - \left[\alpha + g_m(\mu)(1 - \alpha)\right]JF_{Ji}^{-1}p + \phi\bar{\tau}_{ji}.\tag{2.58}$$

Additionally, the spectral decomposition of the stored strain energy for an isotopic solid as described in the work of Miehe et al. (2010) is adopted. The strain energy takes the form,

$$\Omega^+(\varepsilon_{IJ}) = \frac{\lambda^s}{2}\langle\varepsilon_{KK}\rangle^2 + \mu^s\big(\langle\varepsilon_1\rangle^2 + \langle\varepsilon_2\rangle^2 + \langle\varepsilon_3\rangle^2\big)$$

$$\Omega^-(\varepsilon_{IJ}) = -\frac{\lambda^s}{2}\langle-\varepsilon_{KK}\rangle^2 - \mu^s\big(\langle-\varepsilon_1\rangle^2 + \langle-\varepsilon_2\rangle^2 + \langle-\varepsilon_3\rangle^2\big)$$

$$\varepsilon_{IJ} = \frac{1}{2}\big(F_{kI}F_{kJ} - \delta_{IJ}\big)$$

$$(2.59)$$

where λ^s and μ^s are the Lamé material constants, ε_{IJ} is the Green-Lagrangian finite strain measure, and $\varepsilon_{(1,2,3)}$ are the principal strains. If we neglect the (typically small) effects of fluid shear stress and adopt the assumptions of infinitesimal deformations such that $(J-1) \approx \varepsilon_{KK}$ and products of displacement gradients are neglected, the theory recovers linear poroelasticity when the phase-field parameter $\mu = 1$ (and $g_m(\mu = 1) = 0$) (Coussy, 1994; Detournay and Cheng, 1993).

On the contrary, if $\mu = 0$ then $g_m(\mu = 0) = 1$ and there are two important features of the model to note. First, in the presence of an opening strain state, the aggregate stress is $P_{ji} = -JF_{Ji}^{-1}p$ which corresponds to a Cauchy stress of $\sigma_{ji} = -p\delta_{ij}$. Second, the porosity ϕ satisfies $\phi J = \phi_0 + (J-1)$, which implies that $\phi = \phi_0$ in the absence of deformation, and $\phi \to 1$ for large opening deformations as $J \to \infty$. Finally, the rationale for the constraints on the derivative of $g_m(\mu)$ at the endpoints can be understood by considering the micro-force balance in the absence of phase-field gradients and micro-body forces, i.e. when $\bar{\pi} = 0$. For such homogeneous cases if $g'_m(\mu) \neq 0$ at $\mu = 0$ and $\mu = 1$ then the third term in (2.57c) can drive the phase-field parameter outside of the range of $0 \leq \mu \leq 1$.

2.7. The fluid momentum equation and free energy

Generally, as a result of small crack openings, hydraulic fractures are characterized by low Reynolds number flows. In this section the fluid momentum Eq. (2.16) is reduced under the assumptions of isothermal, creeping Newtonian flow. The goal is to simultaneously describe the Darcy-type flow regimes that occur in fully intact regions of the porous aggregate while also properly representing the laminar flow that is present in crack interiors. To this end, the following constitutive relationships are proposed,

$$\tau_{ij} = g_S(\mu)\nu^f\Big[w_{i,j} + w_{j,i} - \tfrac{1}{3}w_{k,k}\delta_{ij} + \phi\Big(v_{i,j} + v_{j,i} - \tfrac{1}{3}v_{k,k}\delta_{ij}\Big)\Big]$$

$$\tilde{f}_i^{sf} = p\big(\phi JF_{Ji}^{-1}\big)_{,J} - \phi_J\tilde{\tau}_{ji} - g_D(\mu)\phi J\frac{\nu^f}{\kappa}w_i.$$

$$(2.60)$$

Here ν^f is the fluid viscosity, κ is the isotropic intrinsic permeability for the aggregate, and $g_S(\mu)$ and $g_D(\mu)$ are indicator functions of the phase-field for the Stokes and Darcy flow regimes. The indicator functions are chosen such that,

$$g_S(\mu) \to 1 \text{ and } g_D(\mu) \to 0 \text{ as } \mu \to 0$$

$$g_S(\mu) \to 0 \text{ and } g_D(\mu) \to 1 \text{ as } \mu \to 1.$$

$$(2.61)$$

The specific forms chosen are,

$$g_S(\mu) = \big(1 - \mu\big)^2$$

$$g_D(\mu) = \mu^n,$$

$$(2.62)$$

where the Stokes function has been chosen based on its simplicity and ease of implementation and the Darcy function is chosen such that the impermeability (which is typically quite high) is degraded more rapidly in the presence of cracks. The choices made for the indicator functions in (2.62) will be shown to reproduce the desired behaviors for the numerical experiments conducted, which will be described in the following sections. In Section 4.4 $n = 4, 6, 8$ will be compared. We note that alternative choices for the indicator functions that comply with (2.61) can be made. However, an exhaustive study of the effects of the form of these functions is beyond the scope of this work. Applying (2.60) and (2.62) within (2.16) and neglecting inertial terms based upon the assumption of low Reynolds number creeping flows, the fluid momentum equation becomes,

$$\Big[g_S(\mu)\nu^f\Big(w_{i,j} + w_{j,i} - \tfrac{1}{3}w_{k,k} + \phi\Big(v_{i,j} + v_{j,i} - \tfrac{1}{3}v_{k,k}\Big)\Big)JF_{Kj}^{-1}\Big]_{,K} - JF_{Ki}^{-1}p_{,K} - Jg_D(\mu)\frac{\nu^f}{\kappa}w_i = 0.$$

$$(2.63)$$

Eq. (2.63) is analogous to Brinkman's equation (Brinkman, 1949) where the material coefficients depend directly on the phase-field parameter μ. When $\mu = 1$ Darcy flow laws are recovered, and when $\mu = 0$ the equations for Stokes flow are recovered.

Additionally, we allow for a compressible fluid and use a linearized relationship between fluid pressure and fluid density to approximate small changes in the fluid density. To this end the following free-energy density for the fluid is proposed,

$$\psi^f = \frac{1}{c^f}\Big(\frac{\rho_0^f}{\rho^f} + \ln\big(\rho^f\big)\Big).$$

$$(2.64)$$

From (2.64) the density pressure relationship becomes,

$$\rho^f = \rho_0^f + c^f p. \tag{2.65}$$

In the absence of the phase-field micro-force balance laws, and the Stokes flow characterization for fluid flow in cracks, the equations presented above reduce to the nonlinear poroelastic theories developed by Coussy and co-workers (Coussy, 1994, 1995, 2010, 1989a, 1989b), which have been shown to be in agreement with Biot's classical theory (Coussy et al., 1998; Biot, 1956; Detournay and Cheng, 1993).

3. Numerical implementation

The numerical experiments presented in the following sections will be for isothermal, isotropic, quasi-static material behavior with steady-state fluid flows. To summarize, the following balance and kinematic equations will enter into the numerical model:

$$P_{Ji,J} + \tilde{b}_i = 0 \quad \text{in } V_0$$
$$P_{Ji}N_J = \tilde{t}_i \quad \text{on } S_t$$
$$u_i = \hat{u}_i \quad \text{on } S_u$$

$$F_{iJ} = \delta_{iJ} + u_{i,J}$$

$$\xi_{I,I} + \tilde{\gamma} + \tilde{\pi} = 0 \quad \text{in } V_0$$
$$\xi_I N_I = \tilde{\iota} \quad \text{on } S_\iota$$
$$\mu = \hat{\mu} \quad \text{on } S_\mu$$

$$\left(\tau_{ji}JF_{Jj}^{-1}\right)_J - JF_{Ji}^{-1}p_J - Jg_D(\mu)\frac{\nu^f}{\kappa}w_i = 0 \quad \text{in } V_0$$
$$\frac{1}{\rho^f}\left(\dot{\phi\rho^f J}\right) + \left(JF_{Ji}^{-1}w_i\right)_J + \frac{\rho_J^f}{\rho^f}JF_{Ji}^{-1}w_i - \tilde{m} = 0 \quad \text{in } V_0$$
$$(\tau_{ji} - p\delta_{ij})JF_{Jj}^{-1}N_J = \tilde{t}_i^f \quad \text{on } S_f$$
$$w_i = \hat{w}_i \quad \text{on } S_w$$
$$p = \hat{p} \quad \text{on } S_p \tag{3.1}$$

Then, the corresponding virtual work statement that will serve as the weak form of these equations for the finite element analysis is,

$$\int_{V_0}\left[P_{Ji}\delta F_{iJ} + \xi_I\delta\mu_I - \tilde{\pi}\delta\mu + \left(\tau_{ji} - pJF_{Jj}^{-1}\right)\delta w_{iJ} + g_D(\mu)\frac{\nu^f}{\kappa}Jw_i\delta w_i - \left(\frac{1}{\rho^f}\left(\dot{\phi\rho^f J}\right) + JF_{Ji}^{-1}w_{iJ} + \frac{\rho_J^f}{\rho^f}JF_{Ji}^{-1}w_i\right)\delta p\right]dV_0$$
$$= \int_{V_0}\left(\tilde{b}_i\delta u_i + \tilde{\gamma}\delta\mu - \tilde{m}\delta p\right)dV_0 + \int_{S_0}\tilde{t}_i\delta u_i dS_0 + \int_{S_0}\tilde{\iota}\delta\mu dS_0 + \int_{S_0}\tilde{t}_i^f\delta w_i dS_0. \tag{3.2}$$

For the numerical method the unknown nodal quantities include the displacements of the aggregate u_i, which is simply the difference between the material point positions in the current and reference configurations, the relative flux of the fluid with respect to the solid w_i, the fluid pressure p, and the phase-field parameter μ. The stresses, P_{Ji} and τ_{ji}, internal micro-forces ξ_i and $\tilde{\pi}$, porosity ϕ, and fluid density ρ^f are determined constitutively from (2.57)–(2.60) and (2.65). We note that the derivations of the governing equations constructed in the previous sections were done so in the reference configuration, which is the domain on which the numerical calculations are performed. The importance in distinguishing between the reference configuration and the current configuration lies in a proper representation of the fluid mass and momentum balances, particularly in regions with degradation. However, for the brittle, linearly elastic materials addressed in this work there is no real advantage in distinguishing the Green-Lagrange strain and its linearized small strain measure. This is due to the fact that the geologically relevant structures investigated in this work undergo relatively small displacements and deformations. In order to simplify the implementation, we believe it is suitable to adopt this small deformation approximation within the stress and micro-force constitutive equations.

In terms of the numerical discretization, standard continuous Galerkin finite element methods are sufficient for the solution of the aggregate equilibrium and micro-force balance equations. Hence, bilinear quadrilateral elements are used to solve these equations. However, for the fluid flow equations it is well-known that the elements must satisfy the LBB

conditions (Ladyshenskaya, 1969; Babuška, 1973; Brezzi, 1974). For the two-dimensional numerical investigations described here we have used Taylor-Hood elements (Taylor and Hood, 1973) with biquadratic interpolations for the relative flux w_i, and bilinear interpolations for the fluid pressure p. The evolution equation that appears in the fluid mass balance is solved using an implicit backward Euler approximation. The fully coupled equations are nonlinear and standard Newton-Raphson procedures are implemented to solve for all quantities of interests simultaneously. This is in contrast with many other phase-field approaches where staggered schemes are used to solve for specific quantities while all other fields are held fixed (Mikelic et al., 2015). For matrix inversion, a parallel, sparse, direct solver from the MUMPS package for the PETSc library is used to solve the problems that are discussed in the next section (Balay et al., 2015; Balay et al., 1997; Amestoy et al., 2001; Amestoy et al., 2006).

4. Results and discussion

This section presents a series of benchmark solutions that the theory must, at a minimum, recover in order to properly model the hydraulic fracture process. Many of these simple solutions are readily recovered if the crack surfaces are identified explicitly by a discrete crack method, but are not trivial for diffuse crack descriptions like the phase-field approach to fracture. The comparison of the model with these foundational problems for which analytical solutions have been developed serves to establish confidence in the theory for when more complex problems are investigated. The three most fundamental problems that are addressed in this paper are the steady, laminar flow through parallel crack faces, the fluid-loading of a free surface as in Terzaghi's consolidation problem, and the uniform pressurization of a plane-strain center crack in an isotropic, impermeable, elastic, infinite solid. After agreement is established for these three fundamental problems, an investigation of the Kristianovic-Geerstma-de Klerk problem (a plane strain center crack in an impermeable, elastic, infinite domain subject to a constant point injection at the crack's center) is carried out. Finally, a problem that includes multiple cracks interacting and merging is presented to demonstrate the advantageous features of the phase-field method.

4.1. Laminar flow between fixed parallel plates

A proper representation of the fluid flow field through the system is needed to produce the correct pressure field. This pressure then drives the solution for the deformation of the aggregate and the evolution of the phase-field within the system. We note that there are also shear stresses within the fluid, but that the influence of fluid shear stress on the aggregate is small. Without a correct representation of the fluid flow, particularly within cracks, an accurate description of crack evolution would be hopeless. Sub-surface cracks are characterized by two long length scales, the crack height and crack length, and one small length scale, the width/opening or crack aperture. Thus, the fluid flow inside the crack is well approximated by the flow between two fixed parallel plates such that the crack walls make up the two plates. Because of the relatively small openings of cracks in these sub-surface materials, the flow is laminar. Assuming the fluid is a Newtonian fluid, the solution to the Navier-Stokes equations for this simplified geometry yields a parabolic flow profile where the total fluid flux through a cross-section per unit crack height is

$$q_y = -\frac{(W_n)^3}{12 \, \nu^f} p_{,y},$$
(4.1)

The result is proportional to the pressure gradient, $p_{,y}$ along the length direction of the crack y (see the inset of Fig. 2), and dependent on the cube of the crack opening aperture $W_n = \Delta u_n$. Thus, it is crucial that the crack opening displacement is properly incorporated into the theory. Due to the fact that the cracks are represented by a diffuse field, Δu_n is not a readily available local quantity for phase-field methods. In order to address this issue, the present theory utilizes a finite deformation framework such that the effects of the crack opening are accounted for in the solution of the fluid flow balances, which are naturally dependent on the deformation within cracks. There is, however, an additional issue that arises for the present theory when numerical discretizations are implemented.

As shown in Fig. 1 the analytic solution to the phase-field theory for fracture has a jump discontinuity in displacement. As previously mentioned, standard Galerkin methods are used to discretize the displacement field u_i, which forces the resulting field to be C° continuous. Thus, the opening in the discretized setting occurs over some discretization length scale associated with the element size, as shown in the figure.

For the discretized case the crack opening width can be estimated as,

$$W_n^h \approx h^e(1 + e_n),$$
(4.2)

where e_n is the nominal strain of a line element perpendicular to the crack plane and h^e is the length scale associated with the discretization. It can be shown that the total crack opening displacement is approximated properly by the discretized method (Bourdin et al., 2012) (i.e. $h^e e_n^h = \Delta u_n^h \approx \Delta u_n$), but, according to (4.2), the actual crack opening width will be over estimated. In order to account for this discrepancy our approach is to use a scaled viscosity defined as,
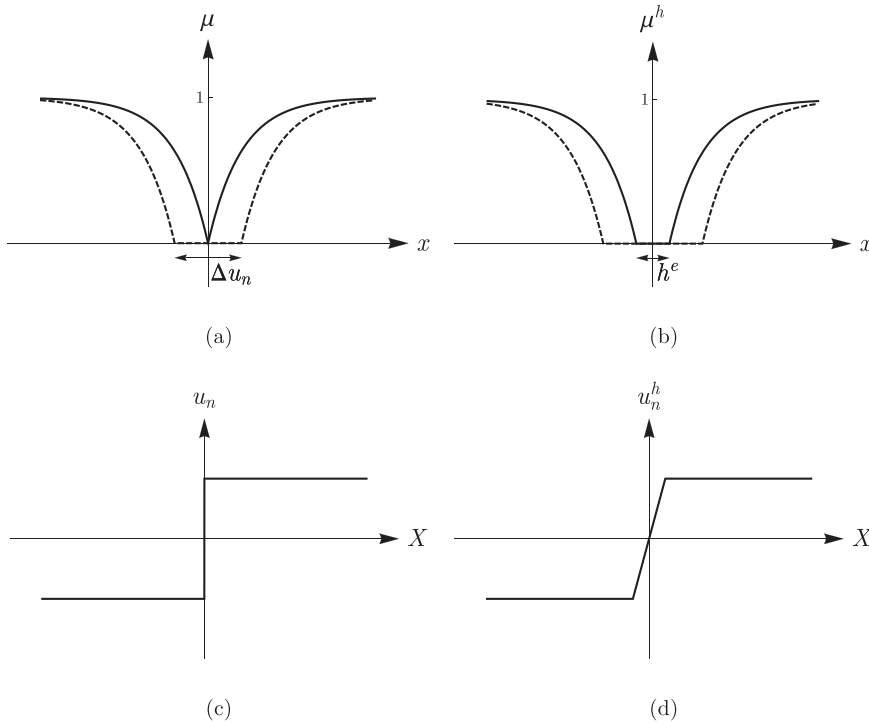
Fig. 1. These plots Illustrate the difference between the analytical and discretized representations of the material stretch normal to a phase-field crack. (a) shows the phase-field profile before deformation (solid line) and after opening (dotted line) in the deformed configuration for the analytical case. (b) shows the phase-field profile before deformation (solid line) and after opening (dotted line) in the deformed configuration for the discretized case. (c) and (d) show the crack opening displacement as a function of location in the reference configuration for the analytical and discretized cases respectively. h^e is a characteristic length scale associated with the discretization (i.e. element size).

$$\nu_s^f = \nu^f \left(\frac{1 + e_n}{e_n} \right)^3 = \nu^f \left(\frac{\lambda_n}{\lambda_n - 1} \right)^3, \tag{4.3}$$

where λ_n is the stretch ratio of a line element perpendicular to the crack plane and can be determined using the deformation gradient F_{iJ} with gradients of the phase-field as,

$$\lambda_n = F_{iJ} n_i N_J = F_{iJ} \frac{\mu_{,i} \mu_{,J}}{\sqrt{\mu_{,k}\mu_{,k}} \sqrt{\mu_{,L}\mu_{,L}}} = \sqrt{\frac{\mu_{,K}\mu_{,K}}{F_{Ik}^{-1} F_{Jk}^{-1} \mu_{,I}\mu_{,J}}}. \tag{4.4}$$

A detailed description of how (4.3) is derived can be found in Appendix A. The viscosity scaling reproduces Reynolds lubrication theory with high fidelity when the crack faces are aligned with element boundaries. However, modest errors do occur when the crack path is oblique to the element boundaries, and this effect is discussed in more detail in Appendix B. Eq. (4.4) is the same measure as that described in Miehe et al. (2015). A simpler approach that does not require the determination of the direction normal to the crack is to utilize the Jacobian of the deformation gradient, which is a reasonable approximation for the normal stretch in highly damaged elements, i.e. $\lambda_n \approx J$. Another potential issue with the scaling (4.3) is that if the stretch is equal to unity or less, the scaled viscosity will approach infinity or become negative. If the phase-field parameter μ is not equal to one in these regions, or the Stokes indicator function $g_S(\mu) > 0$, the scaling as presently proposed will cause issues in the solution of the fluid mass balance (2.63). For instance, as seen in Fig. 1 the stretch is localized to the region of maximum damage, and regions just outside the localization of deformation where the phase-field is still transitioning but the stretch may be unity or less are be subject to the issues described. To address this we restrict the scaling at a value as to not overwhelm Darcy's law. Effectively, a critical stretch λ_c is chosen such that if $\lambda_n < \lambda_c$ the scaling acts as if the crack did not exist and Darcy-like behavior is approximately recovered. The critical stretch is chosen to be $\lambda_c = 1 + 2\sqrt{G_c/E\ell_0}$ which corresponds to roughly 5 times the strain level (Borden et al., 2012) associated with the material peak stress during homogeneous uniaxial straining. Thus, the scaling is chosen such that,

$$\nu_s^f = \nu^f \times \min\left(\left(\frac{\lambda_n}{\langle \lambda_n - 1 \rangle} \right)^3, \left(\frac{\lambda_c}{\lambda_c - 1} \right)^3 \right). \tag{4.5}$$

Note that it is beneficial to the convergence of the Newton-Raphson scheme if there is a smooth transition between these
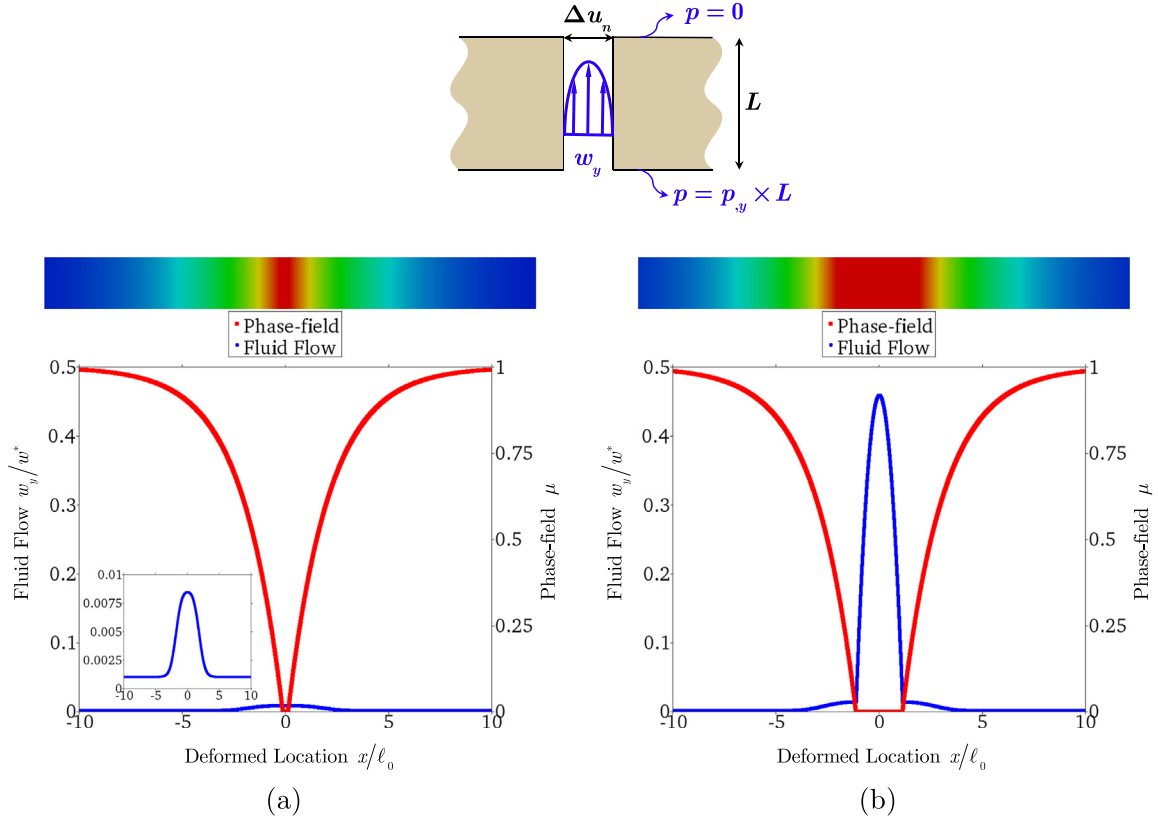
Fig. 2. These simulations demonstrate the ability of the theory to accurately represent the flow through cracks of different openings. A pressure differential is applied between the top and bottom surfaces. The contour plot above shows the phase-field damage profile, which in the undeformed configuration (not shown) is identical for both the open and closed crack. The solutions for the fluid flow in the vertical direction w_y are shown with blue lines for the case of a closed (a) and open (b) diffuse crack. The color contours and red lines indicate the phase-field parameter in the deformed configuration. When the crack is nearly closed (a) there is only enhanced Darcy-like flow (blue line) in the damaged region, as can be seen in the included insert. However, when the crack opens (b) the proper channel flow (blue line) within the crack is recovered such that the net fluid flux is in agreement with laminar flow through fixed parallel plates. The fluid flows (blue line) are normalized by $w^* = -\frac{p_{,y}\ell_0^2}{\nu^f}$. (For interpretation of the references to color in this figure legend, the reader is referred to the web version of this article.).

two limits. One possible construction is detailed in Appendix C. Fig. 2 demonstrates how the flow profile evolves for a given pressure gradient with a large versus a small crack opening. A crack is imposed by setting $\mu = 0$ for a line of elements through the thickness of a thin strip of material. A pressure drop is imposed in the vertical direction and fluid flows through the strip. The flow evolves according to the opening imposed on the crack, starting as an enhanced Darcy-type flow in the region of damage and transitioning to a full Stokes-type flow.

Fig. 3 illustrates how well the dependence on crack opening is captured with and without the viscosity scaling for various element sizes. The total flux through a strip of length $200\ell_0$ is calculated. The volumetric flow rate is normalized by $q^* = -p_{,y}\ell_0^3/\nu^f$ in the plot. The results clearly demonstrate that if the scaling is not used, accuracy cannot be expected unless the crack opening displacement divided by the mesh size, $\Delta u_n^h/h^e$, is well above unity. The solutions for the scaled viscosity deviate slightly from the result for strictly Darcy flow as a result of the enhanced Darcy zone that can be observed in Fig. 2. This is a result of the damage in the neighborhood of the crack and the Darcy degradation function (2.62)b.

A remarkable feature of the viscosity scaling is that there is no explicit dependence on a length scale associated with the discretization. This is in stark contrast with other approaches that utilize the phase-field method to model the hydraulic fracture problem, see (Miehe et al., 2015; Mikelic et al., 2015). The approach adopted in these other models is to use Reynolds lubrication theory directly, i.e. (4.1), by solving the Darcy equation but modifying the permeability based on the crack opening displacement. For instance in Miehe et al. (2015) the approach requires that the stretch normal to the crack plane be multiplied by the square of a length scale associated with the numerical discretization. A similar approach is also used in Mikelic et al. (2015).
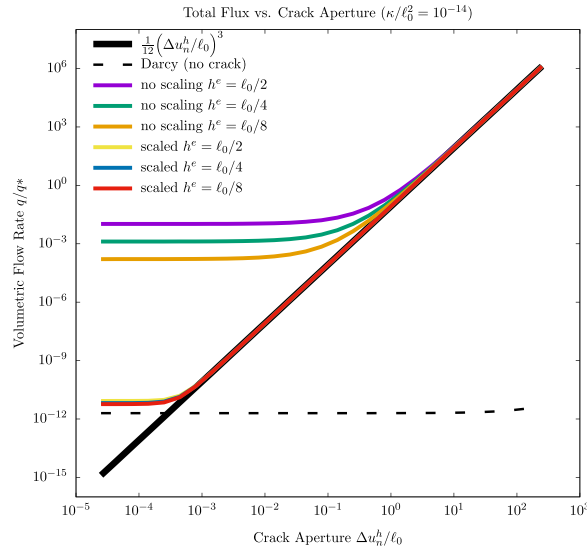
Fig. 3. This plot shows the dependence of the fluid flux on crack opening for the flow through a cracked strip of permeable material. The initial length of the strip is $200\ell_0$ and the middle-most element is completely degraded as in Fig. 1b. The solid black line corresponds to the analytical solution of flow between two fixed, discrete parallel plates (4.1). The purple, green, and orange lines correspond to cases where the fluid viscosity is not scaled for different element sizes. The red, yellow, and blue lines correspond to the scaling (4.5) for various element sizes. The scaling results in excellent agreement with the analytical calculation for crack apertures of practical interest. The damage zone about the crack leads to an enhanced Darcy-type behavior for situations where the crack is essentially closed. This explains the slight discrepancy between the scaled solutions and the Darcy solution (dotted line) where no crack (i.e. no damage) is present. Without the scaling, accurate solutions cannot be expected until the normalized crack aperture is on the order of the mesh size.

4.2. Fluid loading of a surface and consolidation

Perhaps the most classical problem in poromechanics is Terzaghi's consolidation problem (Detournay and Cheng, 1993). A rock or soil layer of thickness L rests on a rigid impermeable base and is subject to a constant applied traction $t_y = -p_0$ on the top surface. The more relevant case for pressurized fractures is the case when the applied load is the consequence of the surface being in contact with a fluid at pressure p_0. For this class of uniaxial strain problems the governing equations for displacement and fluid pressure according to Biot theory can be decoupled. For constant loading, Biot theory reduces to Terzaghi's consolidation theory, which gives a homogenous diffusion equation with constant coefficients for the evolution of the fluid pressure field. Thus, the one-dimensional initial-boundary value problem for fluid pressure can be written as,

$$
\begin{aligned}
&\frac{\partial p}{\partial t} - c\frac{\partial^2 p}{\partial x^2} = 0 && x \in [0, L], \quad t \geq 0 \\
&p = p_0 && x = 0, \quad t \geq 0 \\
&\frac{\partial p}{\partial x} = 0 && x = L, \quad t \geq 0 \\
&p = \frac{(\nu_u - \nu)}{\alpha(1 - 2\nu)(1 - \nu_u)}p_0 && x \in (0, L], \quad t = 0^+
\end{aligned}
$$

$$
c = \frac{2\kappa\mu^s(1 - \nu)(\nu_u - \nu)}{\nu^f\alpha^2(1 - 2\nu)^2(1 - \nu_u)}. \tag{4.6}
$$

Here no distinction is made between the current and reference configurations. The resulting pressure field can be integrated to yield the displacement u_x (see Detournay and Cheng, 1993). The diffusivity coefficient, c, is dependent on the intrinsic permeability, κ, the fluid viscosity, ν^f, the shear modulus of the aggregate, μ^s, the Biot coefficient, α, and the Poisson's ratio of the drained and undrained aggregate, ν and ν_u. Following Detournay (Biot, 1956) and Coussy (Mikelic et al., 2015) the undrained Poisson's ratio ν_u may be determined in terms of the our model parameters as

$$
\nu_u = \frac{3\nu\phi_0(c^f K - 1) + \alpha^2(1 - 2\nu) + 3\alpha\nu(1 + \phi_0)}{3\phi_0(c^f K - 1) - \alpha^2(1 - 2\nu) + 3\alpha(1 + \phi_0)} \tag{4.7}
$$

where we use $c^f = 1/K^f$ and K^f is the bulk modulus of the fluid.

Note that the use of the symbol ν for Poisson's ratios and for viscosity is unfortunate here, but we point this out again to emphasize the distinction. The pore pressure field at the instant of loading corresponds to the homogeneous undrained
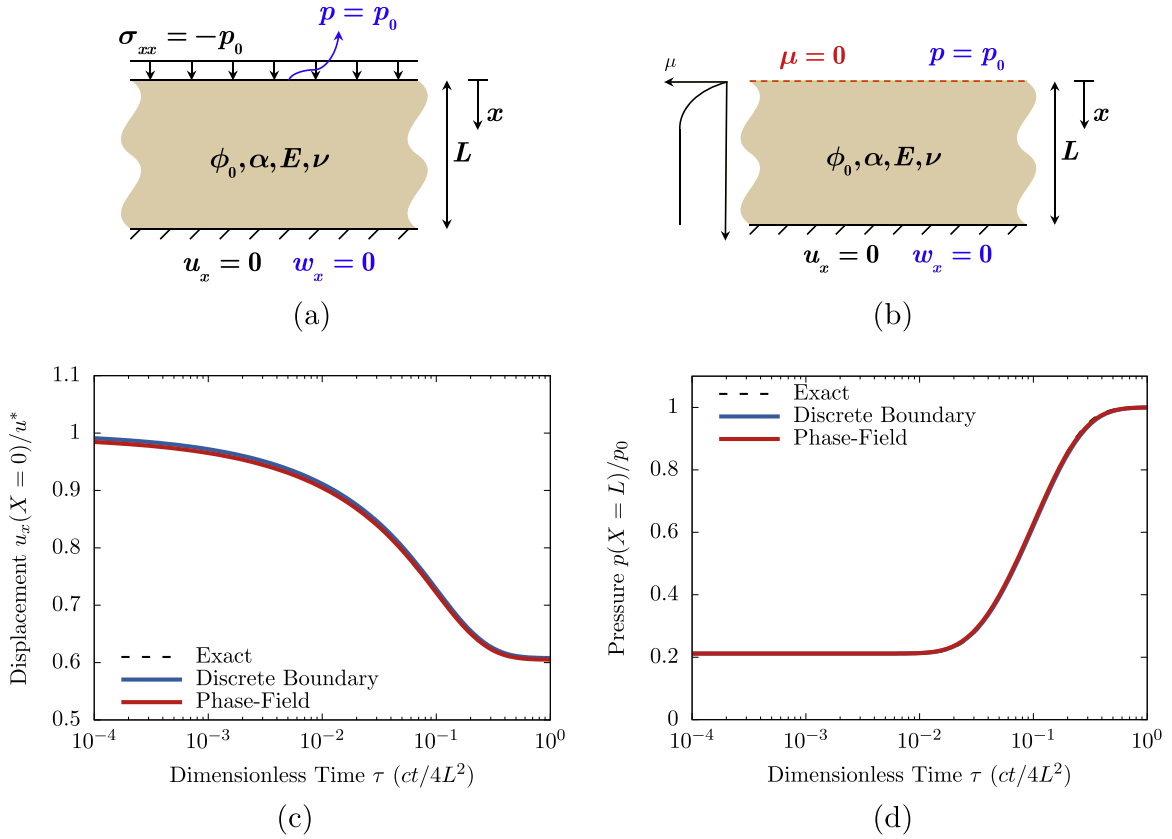
Fig. 4. These plots show the comparison of the phase-field approach(b) to analytical solutions(a) for the time-dependent poroelastic consolidation process. The pore fluid is incompressible. A normal traction is applied to the left boundary or surface ($X = 0$) at time $t = 0^+$ and the surface displacement(c) and pore pressure at the right boundary ($X = L$)(d) are plotted as functions of time. Note that for the phase-field description the left boundary is not a true boundary, but rather is represented by a damaged phase-field. In other words, this can be thought of as the right half of a symmetric pressurized crack. The plots demonstrate excellent agreement with the discrete and analytical solutions to the problem. For these simulations the mesh size is $h^e = \ell_0/4$.

response (i.e. if the material were loaded but fluid was not allowed to enter or leave the system). The reason that this problem is relevant to the phase-field fracture model is that the diffuse phase-field crack surface should act as a permeable boundary. In other words, the solution to (3.1) subject to the following boundary conditions,

$$
\begin{aligned}
\mu &= 0 & & X \leq 0 \ , \ t \geq 0 \\
p &= p_0 & & X \leq 0 \ , \ t \geq 0 \\
w_x &= 0 & & X = L \ , \ t \geq 0 \\
u_x &= 0 & & X = L \ , \ t \geq 0,
\end{aligned}
\tag{4.8}
$$

should approximate the solution to (4.6) for $0 \leq X \leq L$ and $t \leq 0$. Note that in (4.8) the tractions on the crack surface are not specified. Fig. 4 shows the results of calculations when the surface is identified explicitly and when the surface is modeled with the phase-field and compares them with the exact solution provided by Detournay and Cheng (1993). The bulk modulus and fluid compressibility are chosen such that the undrained Poisson ratio is $\nu_u = 0.26$. The other relevant material parameters are taken as $\alpha = 0.45$, $\nu = 0.22$, and $L = 200\ell_0$. On the left plot is the displacement u_x of the surface at $X = 0$ normalized by the initial instantaneous settlement for $t = 0^+$,

$$
u^* = \frac{p_0 L (1 + \nu)(1 - 2\nu_u)}{3K(1 - 2\nu)(1 - \nu_u)},
\tag{4.9}
$$

and on the right plot is the fluid pressure p/p_0 at the impermeable boundary at $X = L$ as each quantity varies over the dimensionless time $\tau = \left(ct/4L^2 \right)$.

The results demonstrate excellent agreement between Biot theory, mixture theory, and the phase-field method developed herein. The only slight discrepancy that can be noticed is that the settlement of the layer at early times is slightly greater for the phase-field formulation. This is due to the fact that the permeability of the aggregate is increased in regions of degradation, and thus, fluid diffusion happens more quickly near the boundary. This behavior only affects the fields in a boundary layer on the order of the fracture surface length scale ℓ_0. In other words, the pressure response far away from the surface is unchanged.
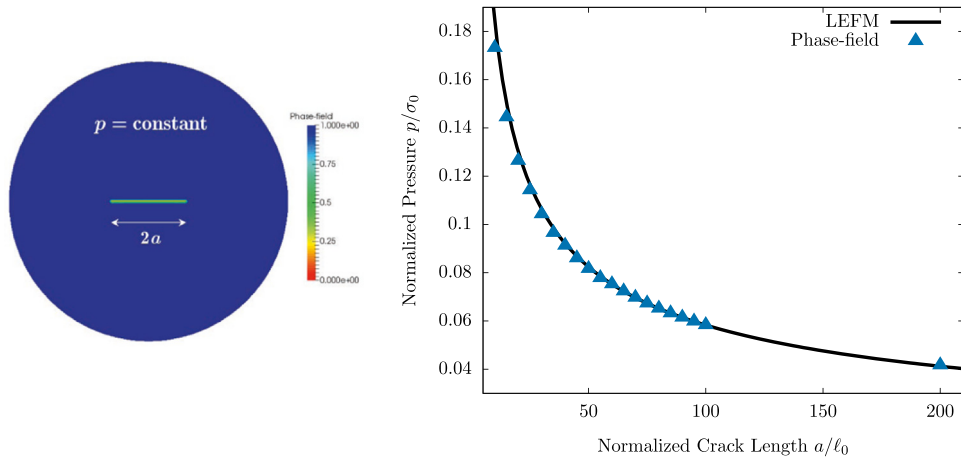
Fig. 5. This plot is a comparison of the phase-field method to the linear elastic fracture mechanics solution for the critical pressure values for propagation of a plane-strain center crack imbedded in an infinite medium. For the phase-field method a crack of given length is designated with Dirichlet boundary conditions and the pressure is increased for the entire mesh until the crack begins to grow unstably. The infinite medium is modeled with a Dirichlet-to-Neumann mapping on the boundary elements of a circular mesh. The phase-field method proposed in this work is in excellent agreement with classical linear elastic fracture mechanics predictions. For these simulations a graded mesh is used with the mesh size in the vicinity of the crack being $h^e = \ell_0/5$, Poisson's ratio $\nu = 0.25$ and $\sqrt{G_c/E\ell_0} = 0.001$.

4.3. Pressurized cracks

The third verification of the model acts to demonstrate that the theory is capable of properly describing the critical pressure loading levels at which cracks within the system should grow. As seen in the previous section, pressurized fluid induces tractions on the crack faces and acts to open up the fractures. The cracks should experience the proper deformation and must propagate at the appropriate critical conditions. To demonstrate that the theory does indeed recover the aforementioned phenomena, a plane-strain center crack in an infinite, isotropic, impermeable, elastic medium is analyzed. If the crack is subject to a uniform pressure then this problem lends itself to a simple linear elastic fracture mechanics solution with which comparisons can be made. The propagation of the crack for fixed pressure conditions is unstable, so the modeling approach is to set a crack at a desired length by imposing that the phase-field be zero along the desired length of elements. Then, the entire system is subject to a uniform pressure that is increased until the crack begins to propagate. The infinite domain is represented with high fidelity by using a Dirichlet-to-Neumann map (Givoli, 1992; Carka et al., 2011) on the outermost boundary of the circular finite element mesh. By conducting the study for various imposed crack lengths, the theory can be verified against the linear elastic fracture mechanics solution. According to linear elastic fracture mechanics, the relationship between the critical pressure and the crack length is,

$$\frac{p_c}{\sigma_0} = \sqrt{\frac{\ell_0}{\pi a}} \tag{4.10}$$

where a is the crack half-length and $\sigma_0 = \sqrt{E'G_c/\ell_0}$.

Fig. 5 shows the results of these calculations. As expected, the phase-field theory reproduces the LEFM result with remarkable accuracy with the exception of when the crack length is short with respect to the length scale ℓ_0. This is to be expected given that the assumption of a small-scale process zone is no longer valid. The length scale ℓ_0 can be shown to be directly analogous to the process zone size from cohesive zone descriptions of cracks like the Dugdale-Barenblatt model. As such, discrepancies arise for short cracks where the process zone length scale becomes significant in relation to the crack length a and this represents a deviation from a regime where linear elastic fracture mechanics is applicable.

4.4. The Kristianovic-Geerstma-de Klerk problem

Now we discuss the apparently simple problem of a plane strain hydraulic fracture in an impermeable, elastic, infinite domain subject to the constant rate injection of an incompressible, Newtonian fluid. This geometry is typically termed the KGD fracture geometry after Geertsma and De Klerk (1969) and Khristianovic and Zheltov (1995). In the last two decades, a group of researchers lead by E. Detournay has revisited this problem, as well as a few other simple geometries like the penny-shaped crack, and conducted state-of-the-art analytical and numerical studies (Detournay, 2004; Detournay and Peirce, 2014; Desroches et al., 1994; Bunger et al., 2005). A concise summary of their results for impermeable rocks can be found in Detournay (2004). A particularly notable result in these works is the introduction of a dimensionless parameter comparing the material fracture toughness to the fluid viscosity,
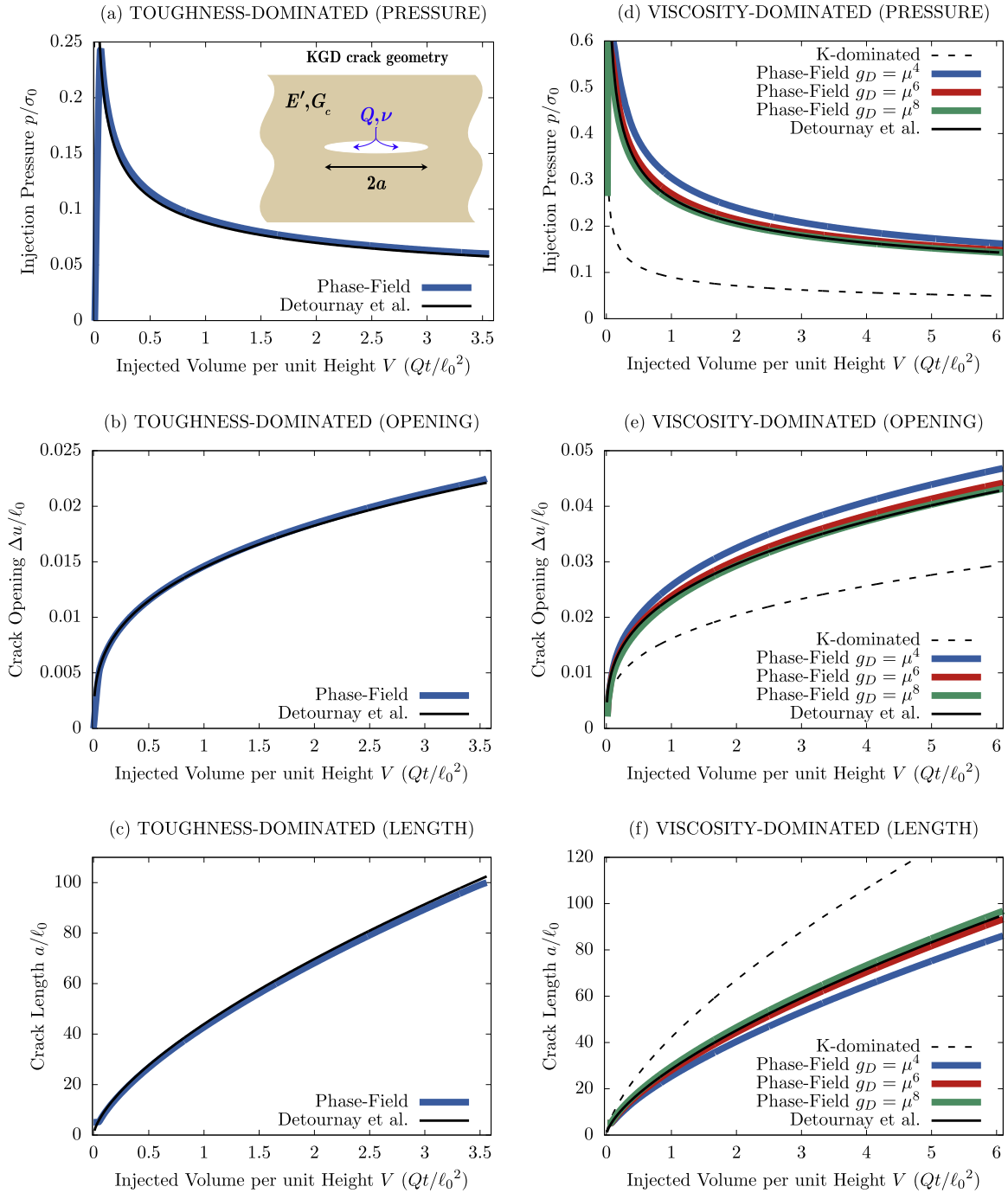
Fig. 6. Phase-field simulation comparisons to the solutions from Detournay (2004) for the 2D KGD crack configuration. (a–c) show results for the toughness-dominated regime $\mathcal{K} = 54.63$, and (d-f) for the viscosity-dominated regime $\mathcal{K} = 0.9714$ for various choices of the Darcy degradation function g_D. Note that models assuming inviscid fluid behavior cannot capture the viscosity dominated regime and would predict behaviors associated with the dashed lines in (d-f). A graded mesh is used with $h^e = \ell_0/5$ in the vicinity of the crack, Poisson's ratio $\nu = 0.25$, $\sqrt{G_c/E\ell_0} = 0.001$, $\ell_0^2/\kappa = 10^{12}$, $(\nu^f Q)/(\sigma_0 \ell_0^3) = 8 \times 10^{-16}$ for (a-c), and $(\nu^f Q)/(\sigma_0 \ell_0^3) = 8 \times 10^{-9}$ for (d-f).

$$\mathcal{K} = 4K_{Ic}\left(3\pi^2 E'^3 Q\nu^f\right)^{-1/4}. \tag{4.11}$$

This dimensionless toughness can be used to delineate the dominating regime of fracture propagation for the KGD crack, toughness versus viscosity-dominated propagation. Based on the assumption that the crack aperture is very small in the systems of interest and inertial terms may be neglected, the hydraulic fracture problem involves two mechanisms of

dissipation that drive the fracture propagation process. In the toughness-dominated regime, where $\mathcal{K} \to \infty$, the energy dissipated by the flow of viscous fluid is small compared to the energy that is dissipated at the crack tip through the creation of new fracture surfaces. In the viscosity-dominated regime, where $\mathcal{K} \to 0$, the energy dissipated by the flow of viscous fluid is far greater than the dissipation due to the creation of new fracture surfaces. In fact, a primary conclusion of Detournay (2004) is that when $\mathcal{K} < 1$ the solution can be accurately approximated by a limit solution constructed on the assumption that the rock has zero toughness, and when $\mathcal{K} > 4$ the solution may be approximated by a limit solution constructed on the assumption that the injected fluid has zero viscosity.

Since no assumptions related to the viscosity or toughness have been made in the construction of this phase-field theory, the model should be able to capture both limiting regimes, as well as the transition between them. Fig. 6 contains plots of the injection pressure, crack opening at the injection site, and crack length results for a plane-strain crack subjected to a constant injection rate for $\mathcal{K} = 54.63$ (toughness-dominated (a)–(c)) and $\mathcal{K} = 0.9714$ (viscosity-dominated (d)–(f)). A small initial crack of half-length $a = 5\ell_0$ is imbedded in an infinite domain (again using a Dirichlet-to-Neumann map on the outer boundary to model the infinite domain) and the crack is subjected to a constant injection rate $\tilde{m}$ at its center. The normal flux of fluid on the outer boundary of the phase-field modeled region is enforced to be zero. For slow enough injection rates, the process resides in the toughness-dominated regime and for high rates of injection, the crack propagates in the viscosity-dominated regime. In each case the functional forms for $g_D(\mu) = \mu^4$, μ^6, and μ^8 were studied. For the toughness-dominated regime the results are effectively independent of $g_D(\mu)$ and the curves for each case are indiscernible. The function $g_D(\mu)$ does play a role in the viscosity-dominated regime as illustrated in Fig. 6. In general, the results are in very good agreement with the limit solutions developed and outlined by Detournay (2004). The slight discrepancies may be explained by the fact that the location of the crack tip is "blurred" since there is a Dugdale-Barrenblatt type of process zone that exists near the tip region in the phase-field model.

The toughness-dominated regime is characterized by uniform pressure in the crack, and thus, the results in this regime correlate to the results where a uniform pressure is imposed for the whole domain. On the other hand, the viscosity-dominated regime is characterized by a non-uniform pressure distribution along the length of the crack. Dotted lines on the viscosity-dominated regime plot illustrate how the crack would behave for the prescribed injection rate if the assumption of uniform pressure were adopted. The difference highlights the necessity of properly modeling the flow within the crack and, in particular, its dependence on crack opening.

Fig. 7 illustrates the comparison between the phase-field calculations for the crack opening and the analytical solution. As with the other quantities characterizing the process in Fig. 6, these plots demonstrate reasonable agreement between the phase-field model and the analytical solutions for the crack opening profiles as a function of time.

4.5. Multiple crack interaction

Here, for illustrative purposes, we show results of a calculation where fluid is injected into a small center crack (half-length $a = 10\ell_0$) that then propagates and merges with two "natural" outer cracks. The overall domain is a rectangle with
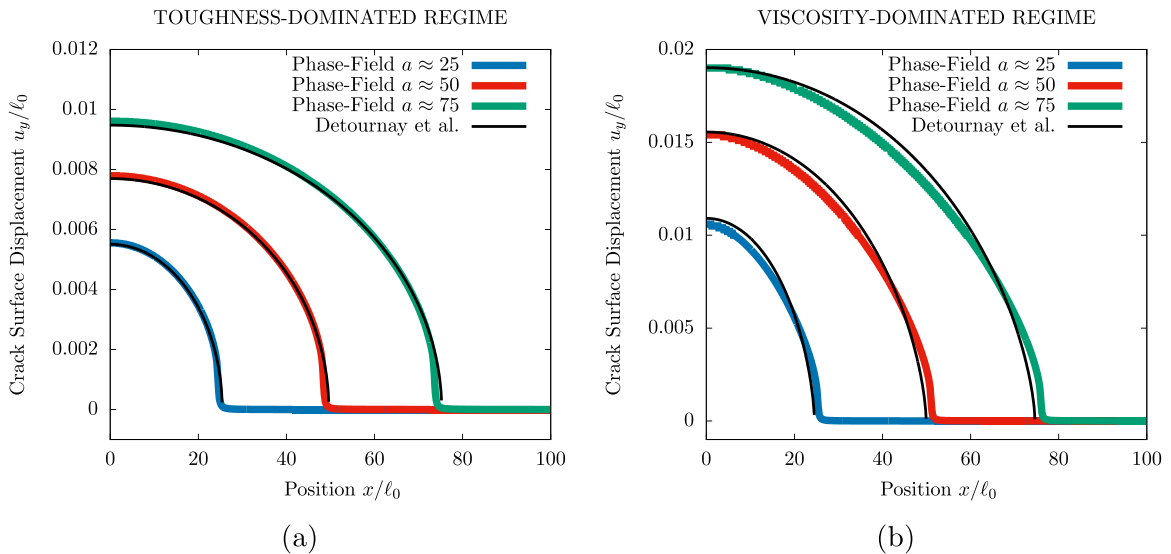

Fig. 7. These plots show comparisons of the phase-field simulation to the solutions from Detournay (2004) for the crack opening profile of the 2D KGD crack configuration. (a) Shows results for three different time steps for a case when fracture toughness is the dominant dissipative mechanism $\mathcal{K} = 54.63$. (b) Shows results for three different time steps for a case when fluid viscosity is the dominant dissipative mechanism $\mathcal{K} = 0.9714$. The Darcy degradation function $g_D(\mu) = \mu^8$ was used for these calculations.
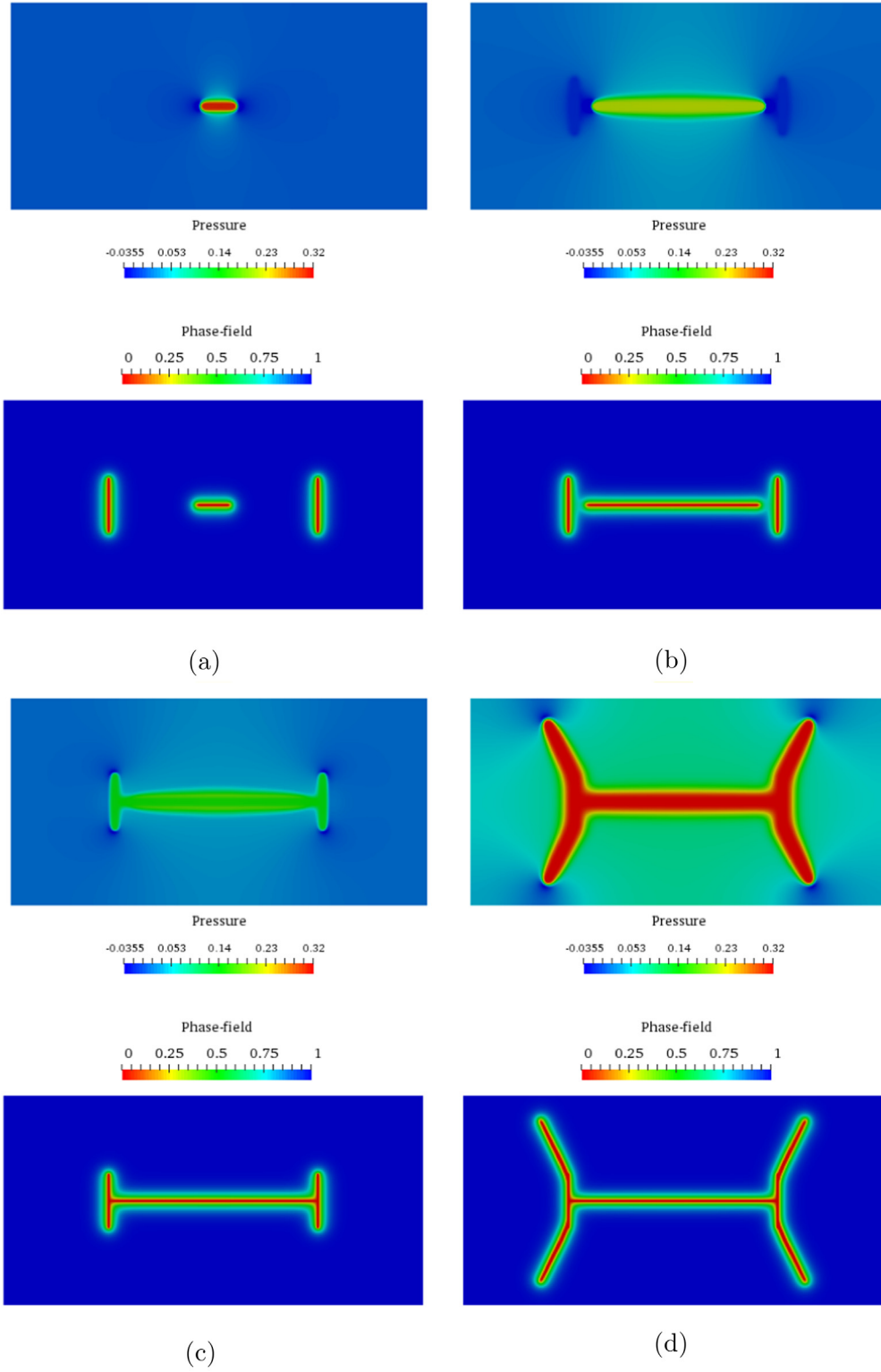
Fig. 8. A merging crack simulation with injection of fluid into the middle crack at a constant rate. Solutions for the fluid pressure and phase-field fracture parameter are shown for four different time steps, (a) $V/\ell_0^3 = 0.1$, (b) $V/\ell_0^3 = 0.85$, (c) $V/\ell_0^3 = 0.9$, and (d) $V/\ell_0^3 = 3.5$. A uniform mesh with $h^e = \ell_0/2$ is used, Poisson's ratio $\nu = 0.25$, $\sqrt{G_c/E\ell_0} = 0.001$, $\ell_0^2/\kappa = 10^{14}$, $\alpha = 0.45$, $\phi_0 = 0.1$, $c^f/\rho_0^f = 0.01364$, and $(\nu^f Q)/(\sigma_0 \ell_0^3) = 5 \times 10^{-12}$.
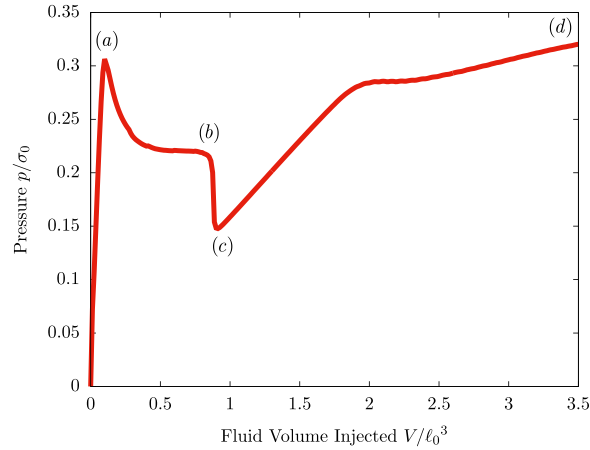
Fig. 9. A plot of the injection pressure versus the volume of fluid injected into the middle crack. The dip in pressure corresponds to the moment that the middle crack merges with the outer cracks. Labels are included that correspond to the snap shots in Fig. 8.

dimensions of $160\ell_0 \times 80\ell_0$. The surface normal displacements and surface normal fluid flux on the outer boundaries are zero. After merging, fluid fills the natural cracks and they begin to propagate from each end in a deflected direction. Contour plots describing the fluid pressure and crack geometry are shown for four different time steps in Fig. 8. For this simulation the Biot coefficient is $\alpha = 0.45$, and the initial porosity is $\phi_0 = 0.1$. As in the consolidation solution, an increase in pore pressure is observed in the undamaged material surrounding the crack. Fig. 9 shows the injection pressure as a function of fluid volume injected into the middle crack. The merging of the three cracks corresponds with a drop in the injection pressure as it takes time for the natural cracks to completely open and fill with fluid. Although it is not necessarily geologically relevant in its simplicity, this simulation provides an example of the capabilities of the modeling approach to capture complex behaviors such as crack merging and non-planar propagation.

5. Summary

This work has outlined the development of a phase-field model for describing the fracturing of a fluid-saturated porous continuum. The governing equations were derived in a general, large deformation framework through the means of fundamental balance laws and Coleman-Noll type procedures. In addition, specific constitutive equations were provided to recover Biot theory in the bulk and incompressible Stokes flow inside cracks. The numerical implementation of these equations was briefly described and several simple solutions were analyzed to verify the expected behavior of the model. With the help of a finite-deformation framework for the governing equations and a mesh-independent viscosity scaling approach, the theory was shown to recover the proper dependence of fluid flow on crack opening displacement. Results were also verified against simple problems in consolidation theory and linear elastic fracture mechanics. Next, the significantly more complex problem of a plane-strain crack subject to uniform fluid injection was investigated. The model was shown to compare favorably to the asymptotic solutions developed by Detournay (2004) for both situations where fracture toughness is the dominant dissipation mechanism and where fluid viscous drag is the dominant dissipation mechanism. Successfully representing both regimes without introducing any regime-dependent constitutive relationships demonstrates the robustness of the modeling approach. Lastly, a model problem that demonstrates the true advantages of a phase-field approach to fracture was described. Crack interactions that resulted in crack path deflection and merging were observed. These phenomena were shown to have a significant impact on fluid injection pressure response. With the confidence established by the favorable comparison to simple analytical solutions, we believe that the phase-field model for fracture can be a powerful tool in understanding many of the more complex behaviors that occur in the hydraulic fracture process.

Acknowledgment

Appendix A

Here we describe the derivation of the viscosity-scaling factor in (4.3). The objective is to obtain equality in flux for two channels of different initial widths, $h^{(1)}$ and $h^{(2)}$, each subjected to the same opening displacement, $\Delta u_n^{h(1)} = \Delta u_n^{h(2)}$, and the same gradient of pressure. Then using (4.1), this implies that,

$$q_y^{(1)} = - \frac{\left(W_n^{h(1)}\right)^3}{12 \ \nu_{(1)}^f} p_y = - \frac{\left(W_n^{h(2)}\right)^3}{12 \ \nu_{(2)}^f} p_y = q_y^{(2)},$$

(A.1)

where $W_n^{h(1,2)} = h^{(1,2)}\left(1 + e_n^{(1,2)}\right)$ as described in Section 4.1. The average nominal strains over the width of each channel are $e_n^{(1)}$ and $e_n^{(2)}$. Since the crack opening displacement for each channel is taken to be equivalent then,

$$\Delta u_n^{h(1)} = \Delta u_n^{h(2)} \Rightarrow e_n^{(1)} h^{(1)} = e_n^{(2)} h^{(2)}.$$

(A.2)

Substituting this into (A.1) and algebraic manipulation gives,

$$\frac{\left(\frac{h^{(1)}}{h^{(2)}} + e_n^{(2)}\right)^3 \left(h^{(2)}\right)^3}{\nu_{(1)}^f} = \frac{\left(1 + e_n^{(2)}\right)^3 \left(h^{(2)}\right)^3}{\nu_{(2)}^f}.$$

(A.3)

Now, if $h^{(1)}$ is taken to represent the idealized case where the initial crack width is zero and $h^{(2)}$ is taken to be the element size in the finite element mesh we find,

$$\nu_{(2)}^f = \nu_{(1)}^f \left(\frac{1 + e_n^{(2)}}{e_n^{(2)}}\right)^3,$$

(A.4)

which is equivalent to (4.3).

Appendix B

The Brinkman type Eq. (2.63), is capable of reproducing Reynold's lubrication theory as described in Section 4.1. This result is critical for the proper modeling of the flow within the crack. The studies conducted in Section 4.1 utilized a uniform mesh with the major axis of the fracture aligned with the structured grid. The results shown in Figures 2 and 3 are characterized by two features of the numerical solution: 1) The deformation within the crack localizes at the element level as discussed earlier and portrayed in Fig. 1. Since quadrilateral bi-linear (Q1) elements were utilized for the displacements the resulting Jacobian of deformation in the cracked elements is constant. 2) The average fluid velocity w_i is discretized using 9-noded bi-quadratic quadrilateral elements (Q2) and, hence the parabolic profile of flow within an element can be represented exactly.

In contrast, when the orientation of the crack does not align with the underlying mesh, the characteristics listed above are not true in general. The deformation within the crack still localizes at the element level; however, the resulting Jacobian is not necessarily constant for the Q1 element. In addition, the parabolic flow profile is not attainable for an element with an arbitrary orientation with respect to the direction along the crack length. Fig. 10 illustrates two distinct types of element-wise deformation for the Q1 element.

The consequence of these responses is that the lubrication theory result of Stokes' equation is not exactly reproduced in these cases and this leads to some solution inaccuracy associated with the mesh orientation dependence. The resulting error may be reduced if an effective element-wise Jacobian is chosen and used in the viscosity scaling Eq. (4.5). It may be chosen as follows,

$$J^{ele} = 0.7 \times \text{avg}[J]_{ele} + 0.3 \times \text{max}[J]_{ele}$$
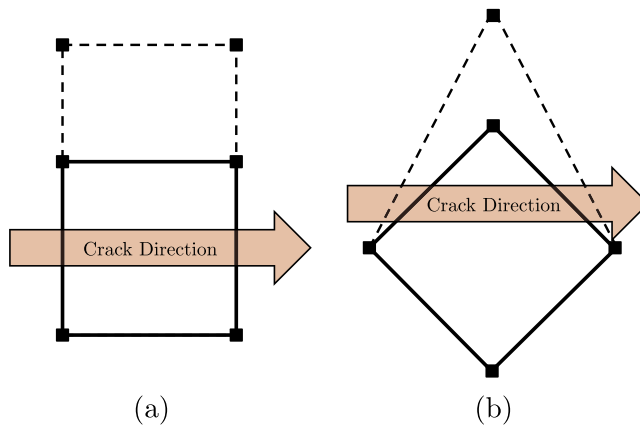
(B.1)

Fig. 10. Representative elements and element deformations. (a) Crack direction is aligned with element orientation. The Jacobian of the deformation gradient is constant. (b) Crack direction is not aligned with element orientation. The Jacobian of the deformation gradient is not uniform for this element.
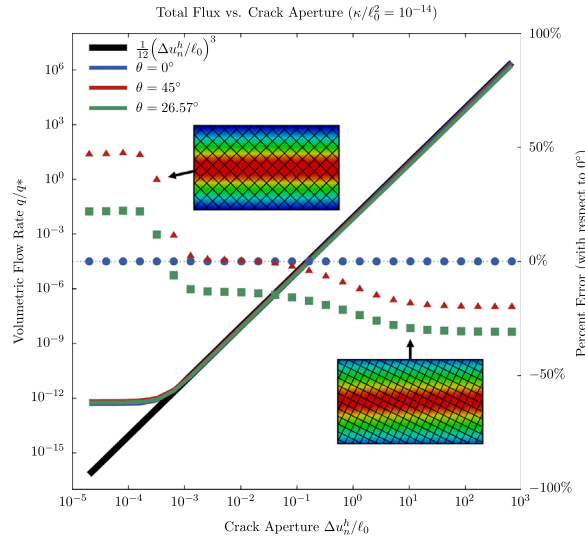
Fig. 11. This figure shows the revisited results of Fig. 3 for cases where the underlying numerical mesh is not oriented in the direction of the crack. The red lines show the results where the element is rotated 45° clock-wise with respect to the crack. The green lines show the results where the element is rotated 26.57° clock-wise with respect to the crack. The blue lines represent a mesh that is oriented in the same direction as the crack. The coefficients in (B.1) were chosen to minimizes the error for the 45° case for reasonable deformations. In both cases, the error is significantly larger for stretches approaching unity and higher. This is a consequence of element distortion. It is important to note that even though some error is introduced by the rotated elements, the overall cubic dependence on crack aperture is maintained. (For interpretation of the references to color in this figure legend, the reader is referred to the web version of this article.).

where the first term indicates the average Jacobian in a given element and the second term indicates the maximum Jacobian in the element, which will always occur at an element corner for the Q1 element. The coefficients were determined empirically based on an element oriented at 45° with respect to the direction of the crack. Clearly the exact point-wise Jacobian is recovered for deformations where the Jacobian is uniform. The calculations performed in Section 4.1, specifically those illustrated in Fig. 3, were performed again for 2 different meshes where the majority of elements were oriented at 45° and 26.57° respectively. The results of those calculations and the meshes themselves are shown in Fig. 11. As can be clearly seen, the presence of elements that are not aligned with the crack gives rise to some error, especially when the deformations are large and the elements become distorted. That being said, the problems studied in this work undergo openings in the range of $\Delta u_n^h / \ell_0 \approx 10^{-3} - 10^{-1}$ corresponding to errors with respect to Reynolds lubrication theory of nearly zero for the 0° orientation, 4% for the 45° orientation, and 15% for the 26.57° orientation within this range of relative openings. Note that even though error is introduced for these discretizations, the cubic dependence of flux on crack aperture is generally maintained. The authors believe that the error that arises for these cases is not an indictment of the general theory but of the underlying numerical discretization. We also believe that more sophisticated numerical schemes or element formulations can be utilized to further reduce these errors, but this is beyond the scope of this paper.

Appendix C

It is advantageous to numerical computations based on Newton-Raphson type schemes to have smooth tangent stiffness components. Thus, convergence results for the coupled N-R scheme can be improved by adopting a smooth rendition of the viscosity scaling outlined by (4.5),

$$\nu_s^f = \nu^f \times \min\left(\left(\frac{\lambda_n}{\langle \lambda_n - 1\rangle}\right)^3, \left(\frac{\lambda_c}{\lambda_c - 1}\right)^3\right). \tag{C.1}$$

Then, a smooth piece-wise scaling function based on λ_c can be defined as,

$$F_\nu(\lambda_n) \equiv \begin{cases} \left(\dfrac{\lambda_c}{\lambda_c - 1}\right)^3 & ; & \lambda_n \leq 1 \\[2ex] \left(\dfrac{\lambda_n(\lambda_n - 2) + (1 - 2\lambda_c)^2}{5 + \lambda_n(\lambda_n - 2) + 4\lambda_c(\lambda_c - 2)}\right)^3 & ; & 1 \leq \lambda_n \leq 2\lambda_c - 1, \\[2ex] \left(\dfrac{\lambda_n}{\lambda_n - 1}\right)^3 & ; & \lambda_n \geq 2\lambda_c - 1 \end{cases}$$

(C.2)

such that a smooth rendition of (4.5) is $\nu_s^f = \nu^f F_\nu(\lambda_n)$.

References

Aamodt, L. & Kuriyagawa, M. (1981). Measurement of instantaneous shut-in pressure in crystalline rock. In: Proceedings of the Presented at the Workshop on Hydraulic Fracturing Stress Measurement, Monterey, Calif., 1–5 Dec. 1981, 1, pp. 1–5.

Adachi, J., Siebrits, E., Peirce, A., Desroches, J., 2007. Computer simulation of hydraulic fractures. Int. J. Rock Mech. Min. Sci. 44, 739–757.

Amestoy, P.R., Duff, I.S., L'Excellent, J.Y., Koster, J., 2001. A fully asynchronous multifrontal solver using distributed dynamic scheduling. SIAM J. Matrix Anal. Appl. 23 (1), 15–41.

Amestoy, P.R., Guermouche, A., L'Excellent, J.Y., Pralet, S., 2006. Hybrid scheduling for the parallel solution of linear systems. Parallel Comput. 32 (2), 136–156.

Amor, H., Marigo, J.J., Maurini, C., 2009. Regularized formulation of the variational brittle fracture with unilateral contact: numerical experiments. J. Mech. Phys. Solids 57, 1209–1229.

Babuška, I., 1973. The finite element method with Lagrangian multipliers. Numer. Math. 20 (3), 179–192.

Balay, S., Gropp, McInnes, L.C., Smith, B.F., 1997. Efficient management of parallelism in object oriented numerical software libraries. Mod. Softw. Tools Sci. Comput., 163–202.

Balay, S., Abhyankar, S., Adams, M.F., Brown, J., Brune, P., Buschelman, K., Dalcin, L., Eijkhout, V., Gropp, W.D., Kaushik, D., Knepley, M.G., McInnes, L.C., Rupp, K., Smith, B.F., Zampini, S., & Zhang, H. (2015). PETSc Users Manual. Argonne National Laboratory, ANL-95/11 – Revision 3.6.

Banks, D., Odling, N.E., Skarphagen, H., Rohr-Torp, E., 1996. Permeability and stress in crystalline rocks. Terra Nova 8, 223–235.

Bell, F.G., 2004. In: Engineering Geology and ConstructionCRC Press.

Bertani, R., 2012. Geothermal power generation in the world 2005–2010 update report. Geothermics 41, 1–19.

Biot, M.A., 1956. The theory of propagation of elastic waves in a fluid saturated porous solid, I. lower frequency range. J. Acoust. Soc. Am. 28, 168–178.

Borden, M.J., Hughes, T.J.R., Landis, C.M., Verhoosel, C.V., 2014. A higher-order phase-field model for brittle fracture: formulation and analysis within the isogeometric analysis framework. Comput. Methods Appl. Mech. Eng. 273, 100–118.

Borden, M.J., Verhoosel, C.V., Scott, M.A., Hughes, T.J.R., Landis, C.M., 2012. A phase-field description of dynamic brittle fracture. Comput. Methods Appl. Mech. Eng. 217–220, 77–95.

Bourdin, B., 2007. Numerical implementation of the variational formulation for quasi-static brittle fracture. Interfaces Free Bound. 9, 411–430.

Bourdin, B., Francfort, G.A., Marigo, J.-J., 2000. Numerical experiments in revisited brittle fracture. J. Mech. Phys. Solids 48, 797–826.

Bourdin, B., Francfort, G.A., Marigo, J.-J., 2008. The variational approach to fracture. J. Elast. 91, 5–148.

Bourdin, B., Larsen, C., Richardson, C., 2011. A time-discrete model for dynamic fracture based on crack regularization. Int. J. Fract. 168, 133–143.

Bourdin, B., Chukwudozie, C., Yoshioka, K., 2012. A Variational Approach to the Numerical Simulation of Hydraulic Fracturing. Society of Petroleum Engineers, SPE159154.

Brezzi, F., 1974. On the existence, uniqueness and approximation of saddle-point problems arising from Lagrangian multipliers. In: Proceedings of the ESAIM: Mathematical Modelling and Numerical Analysis-Modélisation Mathématique et Analyse Numérique, Vol. 8 (R2), pp. 129–151.

Brinkman, H.C., 1949. A calculation of the viscous force exerted by a flowing fluid on a dense swarm of particles. Appl. Sci. Res. 1, 27–34, http://dx.doi.org/10.1007/BF02120313.

Bunger, A.P., Detournay, E., Garagash, D.I., 2005. Toughness-dominated hydraulic fracture with leak-off. Int. J. Fract. 134, 175–190.

Carka, D., Mear, M.E., Landis, C.M., 2011. The Dirichlet-to-Neumann map for two-dimensional crack problems. Comput. Methods Appl. Mech. Eng. 200, 1263–1271.

Chen, L.Q., 2002. Phase-field models for microstructural evolution. Annu. Rev. Mater. Res. 32, 113–140.

Cipolla, C., Weng, X., Mack, M., Ganguly, U., Gu, H., Kresse, O., Cohen, C. (2012). Integrating microseismic mapping and complex fracture modeling to characterize fracture complexity. In: Proceedings of the SPE/EAGE European Unconventional Resources Conference & Exhibition-From Potential to Production.

Coleman, B.D., Noll, W., 1963. The thermodynamics of elastic materials with heat conduction and viscosity. Arch. Rat. Mech. Anal. 13, 245–261.

Coussy, O., 1989a. Thermodynamics of saturated porous solids in finite deformation. Eur. J. Mech. A/Solids 8, 1–14.

Coussy, O., 1989b. A general theory of thermoporoelastoplasticity for saturated materials. Transp. Porous Media 4, 281–293.

Coussy, O., 1994. Poromechanics John Wiley & Sons, Chichester.

Coussy, O., 1995. Mechanics of Porous Continua John Wiley & Sons, Chichester.

Coussy, O., 2010. Mechanics and Physics of Porous Solids John Wiley & Sons, Chichester.

Coussy, O., Detournay, E., Dormieux, L., 1998. From mixture theories to Biot's theory. Int. J. Solids Struct. 35, 4619–4635.

Dahi-Taleghani, A., Olson, J.E., 2011. Numerical modeling of multistranded-hydraulic-fracture propagation: accounting for the interaction between induced and natural fractures. 26. SPE Production & Operations173–184.

Daneshy, A.A., 1973. On the design of vertical hydraulic fractures. J. Pet. Technol. 25, 83–97.

Del Piero, G., Lancioni, G., March, R., 2007. A variational model for fracture mechanics: numerical experiments. J. Mech. Phys. Solids 55, 2513–2537.

Desroches, J., Detournay, E., Lenoach, B., Papanastasiou, P., Pearson, J., Thiercelin, M., & Cheng, A. (1994). The crack tip region in hydraulic fracturing. In: Proceedings of the Royal Society of London. Series A: Mathematical and Physical Sciences, 447, pp. 39–48.

Detournay, E., 2004. Propagation regimes of fluid-driven fractures in impermeable rocks. Int. J. Geomech. 4, 35–45.

Detournay, E., Peirce, A., 2014. On the moving boundary conditions for a hydraulic fracture. Int. J. Eng. Sci. 84, 147–155.

Detournay, E. and Cheng, A.H.-D. (1993). Fundamentals of Poroelasticity, (Chapter 5) in Comprehensive Rock Engineering: Principles, Practice and Projects, Vol. II, Analysis and Design Method, ed. C. Fairhurst, Pergamon Press, pp. 113–171.

Francfort, G.A., Marigo, J.-J., 1998. Revisiting brittle fracture as an energy minimization problem. J. Mech. Phys. Solids 46, 1319–1342.

Fried, E., Gurtin, M.E., 1993. Continuum theory of thermally induced phase transitions based on an order parameter. Physica D. 68, 326–343.

Fried, E., Gurtin, M.E., 1994. Dynamic solid-solid transitions with phase characterized by an order parameter. Physica D 72, 287–308.

Fu, P., Johnson, S.M., Carrigan, C.R., 2013. An explicitly coupled hydro-geomechanical model for simulating hydraulic fracturing in arbitrary discrete fracture networks. Int. J. Numer. Anal. Methods Geomech. 37, 2278–2300.

Geertsma, J., De Klerk, F., 1969. A rapid method of predicting width and extent of hydraulically induced fractures. J. Pet. Technol. 21 (12), 1–571.

Ghassemi, A., 2012. A review of some rock mechanics issues in geothermal reservoir development. Geotechnol. Geol. Eng. 30, 647–664.

Givoli, D., 1992. Numerical methods for problems in infinite domains. In: Studies in Applied Mechanics 33, Elsevier, Amsterdam.

Gu, H., Weng, X., Lund, J.B., Mack, M.G., Ganguly, U., Suarez-Rivera, R. (2011). Hydraulic fracture crossing natural fracture at non-orthogonal angles a criterion its validation and applications. In: Proceedings of the SPE Hydraulic Fracturing Technology Conference. Society of Petroleum Engineers.

Gurtin, M.E., 1996. Generalized Ginzburg-Landau and Canh-Hilliard equations based on a microforce balance. Physica D 92, 178–192.

Ha, Y.D., Bobaru, F., 2010. Studies of dynamic crack propagation and crack branching with peridynamics. Int. J. Fract. 162, 229–244.

Henry, H., Levine, H., 2004. Dynamic instabilities of fracture under biaxial strain using a phase field model. Phys. Rev. Lett. 93, 105504.

Hofacker, M., Miehe, C., 2013. A phase field model of dynamic fracture: robust field updates for the analysis of complex crack patterns. Int. J. Numer. Methods Eng. 93, 276–301.

Karma, A., Kessler, D.A., Levine, H., 2001. Phase-field model of mode III dynamic fracture. Phys. Rev. Lett. 87, 045501.

Khoei, A.R., Haghighat, E., 2001. Extended finite element modeling of deformable porous media with arbitrary interfaces. Appl. Math. Model. 35, 5426–5441.

Khoei, A.R., Vahab, M., Haghighat, E., 2014. A mesh-independent finite element formulation for modeling crack growth in saturated porous media based on an enriched-FEM technique. Int. J. Fract. 188, 79–108.

Khristianovic, S.A., Zheltov, Y.P. (1995). Formation of vertical fractures by means of highly viscous liquid. In: Proceedings of the fourth world petroleum congress, Rome, pp. 579–586.

Koslowski, M., Cuitino, A.M., Ortiz, M., 2002. A phase-field theory of dislocation dynamics, strain hardening and hysteresis in ductile single crystals. J. Mech. Phys. Solids 50, 2597–2635.

Ladyshenskaya, O.A., 1969. In: The Mathematical Theory of Viscous Incompressible Flow2nd ed., Gordon and Breach, New York.

Less, C., Andersen, N., 1994. Hydrofracture: state of the art in South Africa. Appl. Hydrogeol. 2, 59–63.

Lorentz, E., Cuvilliez, S., Kazymyrenko, K., 2012. Modelling large crack propagation: from gradient damage to cohesive zone models. Int. J. Fract. 178, 85–95.

Matek, B., 2015. 2015 annual U.S. & global geothermal power production report. Geotherm. Energy Assoc., 1–21.

Mayerhofer, M.J., Lolon, E., Warpinski, N.R., Cipolla, C.L., Walser, D.W., Rightmire, C.M., 2010. What is Stimulated Reservoir Volume?. 25. SPE Production & Operations89–98.

Meyer, B.R., Bazan, L.W. (2011). A discrete fracture network model for hydraulically induced fractures: theory, parametric and case studies. In: Proceedings of the SPE Hydraulic Fracturing Technology Conference and Exhibition, SPE, 140514.

Miehe, C., Welschinger, F., Hofacker, M., 2010. Thermodynamically consistent phase-field models of fracture: variational principles and multi-field FE implementations. Int. J. Numer. Methods Eng. 83, 1273–1311.

Miehe, C., Mauthe, S., Teichtmeister, S., 2015. Minimization principles for the coupled problem of Darcy-Biot-type fluid transport in porous media linked to phase field modeling of fracture. J. Mech. Phys. Solids 82, 186–217.

Mikelic, A., Wheeler, M.F., Wick, T., 2015. A Phase-field Method for Propagating Fluid-filled Fractures Coupled to a Surrounding Porous Medium. 13. SIAM: Multiscale Modeling and Simulation367–398.

Nordgren, R.P., 1972. Propagation of a vertical hydraulic fracture. Soc. Pet. Eng. J. 12, 306–314.

Olson, J.E., WuK., 2012. Sequential vs. simultaneous multizone fracturing in horizontal wells: insights from a non-planar multifrac numerical model. In: Proceedings of the SPE Hydraulic Fracturing Technology Conference. Society of Petroleum Engineers.

Ouchi, H., Katiyar, A., York, J., Foster, J.T., Sharma, M.M., 2015. A fully coupled porous flow and geomechanics model for fluid driven cracks: a peridynamics approach. Comput. Mech. 55, 561–576.

Pereira, J.P., Duarte, C.A., Jiao, X., 2010. Three-dimensional crack growth with hp-generalized finite element and face offsetting methods. Comput. Mech. 46, 431–453.

Perkins, T.K., Kern, L.R., 1961. Widths of hydraulic fractures. J. Pet. Technol. 13 (09), 937–949.

Provotas, N., Goldenfeld, N., Dantzig, J., 1998. Efficient computation of dendritic microstructures using adaptive mesh refinement. Phys. Rev. Lett. 80, 3308–3311.

Rangarajan, R., Lew, A., 2014. Universal meshes: a method for triangulating planar curved domains immersed in nonconforming meshes. Int. J. Numer. Methods Eng. 98, 236–264.

Rangarajan, R., Chiaramonte, M.M., Hunsweck, M.J., Shen, Y., Lew, A., 2014. Simulating curvilinear crack propagation in two dimensions with universal meshes. Int. J. Numer. Methods Eng. http://dx.doi.org/10.1002/nme.4731.

Roussel, N.P., Sharma, M.M., 2011. Optimizing fracture spacing and sequencing in horizontal-well fracturing. SPE J. 16, 575–581.

Rungamornrat, J., Wheeler, M.F., Mear, M.E. (2005). Coupling of fracture/non-newtonian flow for simulating nonplanar evolution of hydraulic fractures. In: Proceedings of the SPE Annual Technical Conference and Exhibition. Society of Petroleum Engineers.

Settari, A., Cleary, M.P., 1986. Development and testing of a pseudo-three-dimensional model of hydraulic fracture geometry. Soc. Pet. Eng. http://dx.doi.org/10.2118/10505-PA.

Shojaei, A., Taleghani, A.D., Guoqiang, Li, 2014. A continuum damage failure model for hydraulic fracturing of porous rocks. Int. J. Plast. 59, 199–212.

Su, Y., Landis, C.M., 2007. Continuum thermodynamics of ferroelectric domain evolution: theory, finite element implementation, and application to domain wall pinning. J. Mech. Phys. Solids 55, 280–305.

Taylor, C., Hood, P., 1973. A numerical solution of the Navier-Stokes equations using the finite element technique. Comput. Fluids 1, 73–100.

Warpinski, N.R., Mayerhofer, M.J., Vincent, M.C., Cipolla, C.L., Lolon, E.P., 2009. Stimulating unconventional reservoirs: maximizing network growth while optimizing fracture conductivity. J. Can. Pet. Technol. 48, 39–51.

Weng, X., Kresse, O., Cohen, C.-E., Wu, R., Gu, H., 2011. Modeling of hydraulic-fracture-network propagation in a naturally fractured formation. 26. SPE Production & Operations368–380.

Wilson, Z.A., Borden, M.J., Landis, C.M., 2013. A phase-field model for fracture in piezoelectric ceramics. Int. J. Fract. 183, 135–153.

Zhang, W., Bhattacharya, K., 2005. A computational model of ferroelectric domains. Part I: model formulation and domain switching. Acta Mater. 53, 185–198.

Zhang, X., Jeffrey, R.G., 2008. Reinitiation or termination of fluid-driven fractures at frictional bedding interfaces. J. Geophys. Res. 113, B08416.

Zhang, X., Jeffrey, R.G., Thiercelin, M., 2007. Deflection and propagation of fluid-driven fractures at frictional bedding interfaces: a numerical investigation. J. Struct. Geol. 29, 396–410.

Zhang, X., Jeffrey, R.G., Thiercelin, M., 2008. Escape of fluid-driven fractures from frictional bedding interfaces: a numerical study. J. Struct. Geol. 30, 478–490.